PAPER

Homoclinic saddle to saddle-focus transitions in 4D systems

IOP Publishing | London Mathematical Society Nonlinearity

Nonlinearity **32** (2019) 2024–2054 https://doi.org/10.1088/1361-6544/ab0041

Homoclinic saddle to saddle-focus transitions in 4D systems

Manu Kalia[1], Yuri A Kuznetsov[1,2] and Hil G E Meijer[1]

[1] Department of Applied Mathematics, University of Twente, Zilverling Building, PO Box 217, 7500AE Enschede, The Netherlands
[2] Mathematical Institute, Utrecht University, Budapestlaan 6, 3584CD Utrecht, The Netherlands

E-mail: M.Kalia@utwente.nl, I.A.Kouznetsov@uu.nl and H.G.E.Meijer@utwente.nl

Received 23 April 2018, revised 14 January 2019
Accepted for publication 21 January 2019
Published 3 May 2019

Recommended by Dr Hinke M Osinga

Abstract

A saddle to saddle-focus homoclinic transition when the stable leading eigenspace is three-dimensional (called the 3DL bifurcation) is analyzed. Here a pair of complex eigenvalues and a real eigenvalue exchange their position relative to the imaginary axis, giving rise to a 3D stable leading eigenspace at the critical parameter values. This transition is different from the standard Belyakov bifurcation, where a double real eigenvalue splits either into a pair of complex-conjugate eigenvalues or two distinct real eigenvalues. In the wild case, we obtain sets of codimension 1 and 2 bifurcation curves and points that asymptotically approach the 3DL bifurcation point and have a structure that differs from that of the standard Belyakov case. We give an example of this bifurcation in a perturbed Lorenz–Stenflo 4D ordinary differential equation model.

Keywords: homoclinic bifurcations, numerical bifurcation analysis, bifurcation theory
Mathematics Subject Classification numbers: 34C37, 37G20, 65P30

(Some figures may appear in colour only in the online journal)

1. Introduction

Homoclinic orbits play an important role in the analysis of ordinary differential equations (ODEs) depending on parameters

$$\dot{x} = F(x, \alpha), \quad x \in \mathbb{R}^n, \alpha \in \mathbb{R}^m, \tag{1}$$

where F is sufficiently smooth in both phase components and parameters. Orbits homoclinic to *hyperbolic equilibria* are of specific interest, as they are structurally unstable, and the corresponding parameter values generically belong to codim 1 manifolds in the parameter space $\mathbb{R}^m$. Bifurcations in generic one-parameter families transverse to such manifolds depend crucially on the configuration of *leading eigenvalues* of the equilibrium, i.e. the stable eigenvalues with largest real part, and the unstable eigenvalues with smallest real part.

In figure 1, we see three configurations with simple leading eigenvalues, for which a detailed description of the bifurcations occurring near the homoclinic orbit is available (see, e.g. [1–4]). For example, in the saddle case, a single periodic orbit appears generically. In the saddle-focus case, we can assume that the leading stable eigenvalues are complex by applying time-reversal if necessary. In this case, infinitely many periodic orbits exist if the *saddle quantity* σ_0, defined as the sum of the real part of the leading unstable and stable eigenvalues, is positive. This phenomenon is called *Shilnikov's homoclinic chaos* [5, 6]. On the contrary, if σ_0 is negative, then generically only one periodic orbit appears. Thus, the sign of σ_0 distinguishes *wild* and *tame* saddle-focus homoclinic cases. Note that in the wild case many other bifurcations occur nearby, including infinite sequences of fold (limit point, LP) and period-doubling (PD) bifurcations of periodic orbits, as well as secondary homoclinic bifurcations, which all accumulate on the primary homoclinic bifurcation manifold [7]. In the focus–focus case, which will not be considered in this paper, infinitely many periodic orbits are always present.

Moving along the primary homoclinic manifold in the parameter space of (1), one may encounter a transition from the saddle case (a) to the saddle-focus case (b). This is a degenerate situation, and the corresponding homoclinic parameter values generically form a codim 2 sub-manifold in the parameter space. Nearby bifurcations should be studied using generic two-parameter families transverse to this codim 2 sub-manifold. We can therefore restrict ourselves to generic two-parameter ODEs ($m = 2$), where the primary homoclinic orbit exists along a smooth *homoclinic curve* in the parameter plane, while the saddle to saddle-focus transition happens at an isolated point on this curve. There are many more codim 2 homoclinic bifurcations, see [3, 4, 8].

As already noted in [8], at the simplest saddle to saddle-focus transition we have either

(i) a *double* leading eigenvalue; or
(ii) *three simple* leading eigenvalues.

In case (i), see figure 2, the pair of leading complex eigenvalues approaches the real axis and splits into two distinct real eigenvalues. At the transition there is a double real eigenvalue and the leading eigenspace is 2D. In case (ii), see figure 3, the real eigenvalue exchanges its position with the pair of complex-conjugate eigenvalues. At the transition there are two complex-conjugate eigenvalues and one real eigenvalue with the same real part. All leading eigenvalues are simple and the leading eigenspace is 3D.

Case (i) is a saddle to saddle-focus homoclinic transition that appears in various applications, e.g. in biophysics [9] and ecology [10]. Moreover, in these applications the transition corresponds to the wild case with $\sigma_0 > 0$. This case was first studied analytically by Belyakov [11], who proved that the corresponding bifurcation diagram is complicated. We call this case

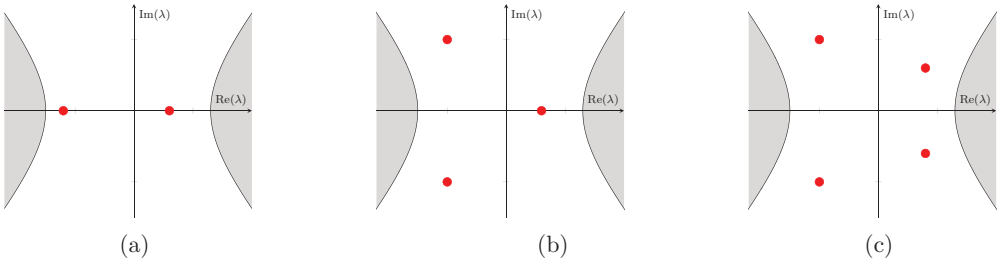

Figure 1. Configurations of leading eigenvalues λ (red). Gray area contains all non-leading eigenvalues. (a) Saddle. (b) Saddle-focus. (c) Focus–focus.

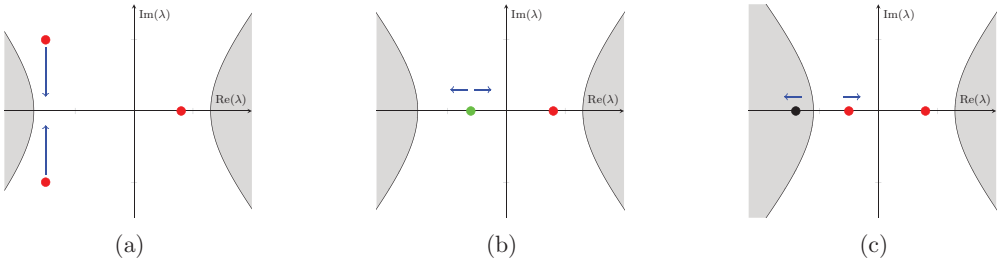

Figure 2. Eigenvalue configurations of the saddle to saddle-focus transition in case (i); α is the parameter along the homoclinic curve and the bifurcation occurs at $\alpha = 0$. Arrows point in the direction of generic movement of eigenvalues. The green marker indicates a double real eigenvalue. The gray areas contain non-leading eigenvalues, leading eigenvalues are marked red and non-leading eigenvalues are marked black. (a) $\alpha < 0$. (b) $\alpha = 0$. (c) $\alpha > 0$.

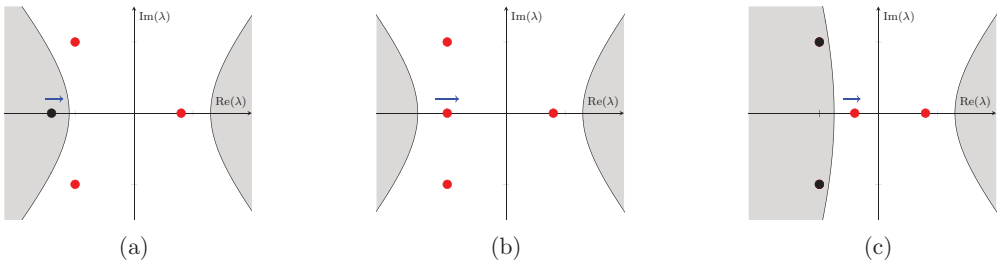

Figure 3. Eigenvalue configurations of the saddle to saddle-focus transition in case (ii); the scalar bifurcation parameter along the homoclinic curve is α. Arrows point in the direction of possible movement of eigenvalues. There is a codimension 2 situation at $\alpha = 0$, where the leading stable eigenspace becomes 3D. Non-leading eigenvalues are contained in the gray area, leading eigenvalues are marked red and non-leading eigenvalues are marked black. (a) $\alpha < 0$. (b) $\alpha = 0$. (c) $\alpha > 0$.

the *standard Belyakov case*. In [10, 11] a description of the main features of the universal bifurcation diagram close to this transition for $n = 3$ in the wild case has been obtained:

1. There exists an infinite set of LP and PD bifurcation curves.
2. There exists an infinite set of *secondary homoclinic* curves corresponding to homoclinic orbits making two global excursions and various numbers of local turns near the equilibrium.

3. Both sets have the same 'bunch' shape: the corresponding curves emanate from the codim 2 point and accumulate onto the branch of primary saddle-focus homoclinic orbits. The secondary homoclinics accumulate only from one side.

Case (ii) has recently been observed in [12] for a 4D system of ODEs arising from a study of traveling waves in a neural field model. We will revisit this model in section 6, only noting here that the transition in this model is tame with $\sigma_0 < 0$. As in the standard Belyakov case, we expect a complicated bifurcation diagram in the wild case, i.e. when $\sigma_0 > 0$.

Our paper is devoted to the theoretical analysis of the homoclinic saddle to saddle-focus transition for case (ii), when the leading stable eigenspace is 3D. We call this transition the *3DL transition* and mainly consider the wild case. To the best of our knowledge, no systematic analysis of this case is available in the literature, and it is one of the few remaining untreated codim 2 homoclinic bifurcations in ODEs, see [4] for a review. A possible reason for this gap is that case (ii) can only occur in (1) with $n \geqslant 4$, while case (i) happens already in 3D ODEs. This leads to the study of a 3D return map in case (ii), which is much more difficult to analyze than the planar return map in the standard Belyakov case (i).

By considering a generic 4D system with the 3DL transition, we are able to obtain a two-parameter model 3D return map which describes the bifurcations occurring close to the transition. We will see that in the wild case $\sigma_0 > 0$, there exist infinitely many bifurcation curves. However, the shape of these bifurcation curves differs essentially from those in the standard Belyakov case (i):

1. There exist infinitely many PD, LP, torus (Neimark–Sacker, NS) and secondary homoclinic curves. These curves accumulate onto the curve of primary homoclinic orbits but do not emanate from the codim 2 point.
2. Each LP curve is a 'horn' composed of two branches. Close to the horn's tipping point LP and PD curves are organized via *spring* and *saddle areas* [13]. Transitions between the saddle and spring areas are observed. Each secondary homoclinic curve forms a 'horizontal parabola'.
3. Several codim 2 points exist on each of the LP, PD and NS curves. We observe generalized period-doubling (GPD) and cusp (CP) points, as well as strong resonances.

Using the model map, we prove analytically that the cusp points asymptotically approach the wild 3DL transition point. The same is shown for the secondary homoclinic turning points. We present numerical evidence that all other mentioned codimension 2 points form sequences also converging to the 3DL transition point.

This paper is organized as follows. In section 2 we formulate the genericity assumptions on (1) with $n = 4$ and $m = 2$. Next, we derive a model 3D return map and its 1D simplification. In section 3 we analyze the 1D model map to describe LP and PD bifurcations of the fixed points/periodic orbits. An essential part of the analysis of the 1D map is carried out analytically, while that of the full 3D model map in section 4 employs advanced numerical continuation tools, except for the LP and PD bifurcations (reducible to the 1D return map studied in section 3) and the secondary homoclinic bifurcations. In section 5, implications for the dynamics of the original 4D ODE system are summarized. Finally, in section 6, we give explicit examples of tame and wild 3DL transitions in concrete models. The tame example is a system that describes traveling waves in a neural field. The wild example is a perturbed Lorenz–Stenflo model appearing in atmospheric studies. Various issues, including generalization to higher dimensions, are discussed in section 7.

2. Derivation of the model maps

2.1. Assumptions

We make the following assumptions about the 3DL transition at the critical parameter values, which we assume to be $\alpha_1 = \alpha_2 = 0$. Recall that we only consider $n = 4$ and $m = 2$.

(A.1) The eigenvalues of the linearization at the critical 3DL equilibrium $x = 0$ are

$$\delta_0, \delta_0 \pm \mathrm{i}\omega_0 \text{ and } \epsilon_0,$$

where $\delta_0 < 0, \omega_0 > 0$ and $\epsilon_0 > 0$.

(A.2) There exists a homoclinic orbit Γ_0 to this 3DL equilibrium, called the *primary homoclinic orbit*.

(A.3) The homoclinic orbit Γ_0 does not exhibit an additional orbit-flip: The normalized tangent vector to Γ_0 has nonzero projections to both the 1D eigenspace corresponding to the real eigenvalue δ_0 and to the 2D eigenspace corresponding to the complex eigenvalues $\delta_0 \pm \mathrm{i}\omega_0$, when approaching the equilibrium.

Any system (1) with $(n, m) = (4, 2)$ and satisfying the assumptions **(A.1–3)**, can be transformed near the critical equilibrium via a translation, a linear transformation, a linear time scaling, and introducing new parameters $\mu = (\mu_1, \mu_2)$, to

$$\dot{x} = \Lambda(\mu)x + g(x, \mu), \qquad x \in \mathbb{R}^4,\ \mu \in \mathbb{R}^2, \tag{2}$$

where

$$\Lambda(\mu) = \begin{pmatrix} \gamma(\mu) & -1 & 0 & 0 \\ 1 & \gamma(\mu) & 0 & 0 \\ 0 & 0 & \gamma(\mu) - \mu_1 & 0 \\ 0 & 0 & 0 & \beta(\mu) \end{pmatrix}, \tag{3}$$

and the smooth vector-valued function $g(x, \mu)$ vanishes together with its derivative w.r.t. x at $x = 0$ for all $\mu \in \mathbb{R}^2$ sufficiently small, and

$$\gamma(0) = \frac{\delta_0}{\omega_0} \text{ and } \beta(0) = \frac{\epsilon_0}{\omega_0}. \tag{4}$$

Define

$$\nu(\mu) := -\frac{\gamma(\mu)}{\beta(\mu)} \tag{5}$$

and let $\gamma_0 := \gamma(0)$ and $\beta_0 := \beta(0)$. The number

$$\nu_0 = \nu(0) = -\frac{\gamma_0}{\beta_0} = -\frac{\delta_0}{\epsilon_0} \tag{6}$$

is called the *saddle index*. Note that the saddle quantity σ_0 introduced earlier is related to the saddle index (6) as follows:

$$\nu_0 < 1 \Longleftrightarrow \sigma_0 > 0,$$
$$\nu_0 > 1 \Longleftrightarrow \sigma_0 < 0.$$

We assume from now on that $\nu_0 < 1$, so that only the wild case $\sigma_0 > 0$ is considered.

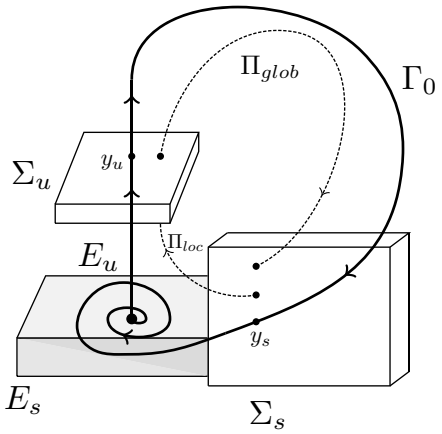

Figure 4. The choice of cross-sections close to the critical 3DL saddle at $(0,0,0,0)$ and the homoclinic connection Γ_0, in order to obtain the map $\Pi : \Sigma_s \to \Sigma_s$. Here Σ_u is defined by the cross-section $v = d_u$ and Σ_s is the cross-section $u_2 = 0$. The homoclinic connection is assumed to pass through the points $y_s = (d_s, 0, \tilde{d}_s, 0)$ and $y_u = (0,0,0,d_u)$. The stable and unstable invariant manifolds locally coincide with the eigenspaces E_s and E_u, respectively.

In system (2), $\mu_2 = \mu_2(\alpha)$ is a 'splitting function' so that the primary homoclinic orbit to the equilibrium (saddle, 3DL, saddle-focus) exists along the curve $\mu_2 = 0$. The exact choice of μ_2 will be clarified later. The value $\mu_1(\alpha)$ controls which stable eigenvalue leads. For $\mu_1 > 0$, the stable leading eigenvalues are complex (saddle-focus case) and for $\mu_1 < 0$ the stable leading eigenvalue is real (saddle case).

Now we can formulate the final (transversality) assumption:

(A.4) The components of $\mu = (\mu_1, \mu_2)$ are small and the 3DL saddle exists at $\mu = 0$. Moreover, the mapping $\alpha \mapsto \mu(\alpha)$ is regular at $\alpha = 0$, i.e. $D\mu(0)$ is nonsingular.

2.2. Introducing cross-sections

Our next aim is to derive the model Poincaré map close to Γ_0 near the 3DL transition, that we will use for the two-parameter perturbation study.

Using the Ovsyannikov–Shilnikov theorem [3, 14] (see also [15–17]) and a time reparameterization, we can conclude that (2) is smoothly orbitally equivalent in a neighborhood of $x = 0$ to

$$\begin{cases} \dot{u} &= A(\mu)u + f(u,v,\mu)u, \\ \dot{v} &= \beta(\mu)v, \end{cases} \tag{7}$$

where $u = (u_1, u_2, u_3) \in \mathbb{R}^3, v \in \mathbb{R}$,

$$A(\mu) = \begin{pmatrix} \gamma(\mu) & -1 & 0 \\ 1 & \gamma(\mu) & 0 \\ 0 & 0 & \gamma(\mu) - \mu_1 \end{pmatrix}, \tag{8}$$

and, for all sufficiently small $\mu \in \mathbb{R}^2$, the (3×3)-matrix-valued function f vanishes at $u_1 = u_2 = u_3 = v = 0$ and, moreover, $f(u,0,\mu) = 0$ for all $u \in \mathbb{R}^3$ with sufficiently small $\|u\|$, while $f(0,v,\mu) = 0$ for all sufficiently small $|v|$. Note that in general (7) is only C^{k-2}-smooth in (u,v,μ) even if the original system (2) is C^k.

Figure 4 gives an impression of the homoclinic connection to a 3DL saddle in the 4D system (7). As we are interested in understanding the bifurcations close to the homoclinic orbit, we define two Poincaré cross-sections,

$$\Sigma_s = \{(u_1, u_2, u_3, v) | u_2 = 0\}, \tag{9}$$

$$\Sigma_u = \{(u_1, u_2, u_3, v) | v = d_u\}, \tag{10}$$

and assume that the homoclinic orbit passes through these cross-sections at $y_s = (d_s, 0, \tilde{d}_s, 0)$ and $y_u = (0, 0, 0, d_u)$, respectively, for all parameter values along the primary homoclinic curve, where $d_s, \tilde{d}_s$ and d_u are sufficiently small but positive. This is possible due to assumption **(A.3)**, which also guarantees that the primary homoclinic orbit does not exhibit an orbit-flip.

Clearly, both cross-sections are transversal to the flow and to the stable and unstable eigenspaces. Thus, by following orbits starting from Σ_s to Σ_u and returning back to Σ_s, we can define a 3D map Π mapping (a subset of) Σ_s to itself. We will use this map to study both periodic orbits and secondary homoclinic orbits.

We shall construct the map Π by composing two maps, $\Pi_{\text{loc}} : \Sigma_s \to \Sigma_u$ and $\Pi_{\text{glob}} : \Sigma_u \to \Sigma_s$, i.e.

$$\Pi = \Pi_{\text{glob}} \circ \Pi_{\text{loc}}. \tag{11}$$

We want to construct a solution of (7) that starts at $t = 0$ from a point $x_0 \in \Sigma_s$ close to y_s and arrives at a point $x_\tau \in \Sigma_u$ close to y_u at some $t = \tau > 0$. This solution will be used to define the local map Π_{loc}.

2.3. Derivation of the return map

Following the classical approach by Shilnikov [3, 14], consider the integral equation on $[0, \tau]$:

$$\begin{cases} u(t) = \mathrm{e}^{At} u_0 + \int_0^t \mathrm{e}^{A(t-s)} f(u, v, \mu) u(s) \mathrm{d}s, \\ v(t) = \mathrm{e}^{-\beta(\tau - t)} v_\tau, \end{cases} \tag{12}$$

where $\tau > 0$ is some constant. Let $\epsilon > 0$ be sufficiently small, and let $\tau > 1/\epsilon$. Given any $(u_0, v_\tau) \in \mathbb{R}^4$ with $\|u_0\| + |v_\tau| < \epsilon$, a unique solution $(u(t), v(t))$ satisfying the above integral equation for $t \in [0, \tau]$ can be obtained by successive approximations. The resulting solution $x(t) = (u(t), v(t))$ satisfies (7) with $u(0) = u_0$ and $v(\tau) = v_\tau$, and depends (as smoothly as (7)) on τ, as well as on (u_0, v_τ) and μ (see [4, 14]).

This solution will be used to define the local map Π_{loc} that sends $x_0 = (x_1^s, 0, x_3^s, x_4^s) \in \Sigma_s$ to a point $x_\tau = (x_1^u, x_2^u, x_3^u, d_u) \in \Sigma_u$, i.e. when $u_0 = (x_1^s, 0, x_3^s)$ and $v_\tau = d_u$. We now write $x(t)$ in a more explicit form.

First, by linearly scaling the phase variables, we transform (7) to

$$\begin{cases} \dot{x_1} = \gamma(\mu) x_1 - x_2 + \frac{1}{d_s} \sum_{j=1}^3 f_{1j}(\tilde{x}, \mu) \tilde{x}_j, \\ \dot{x_2} = x_1 + \gamma(\mu) x_2 + \frac{1}{d_s} \sum_{j=1}^3 f_{2j}(\tilde{x}, \mu) \tilde{x}_j, \\ \dot{x_3} = (\gamma(\mu) - \mu_1) x_3 + \frac{1}{\tilde{d}_s} \sum_{j=1}^3 f_{3j}(\tilde{x}, \mu) \tilde{x}_j, \\ \dot{x_4} = \beta(\mu) x_4, \end{cases} \tag{13}$$

where $\tilde{x} = (d_s x_1, d_s x_2, \tilde{d}_s x_3, d_u x_4)$. Note that the homoclinic orbit now passes through $y_s = (1, 0, 1, 0)$ and $y_u = (0, 0, 0, 1)$, since Σ_u is now characterized by $x_4 = 1$.

It follows from [4, 14] that the solution $x(t)$ of (13) can be written for sufficiently small $\|\mu\|$, as

$$x(t) = \begin{pmatrix} x_1^s \mathrm{e}^{\gamma(\mu)t}\left[(1+\tilde{\varphi}_{11})\cos(t) + \tilde{\varphi}_{12}\sin(t) + o\left(\mathrm{e}^{\gamma(\mu)t}\right)\right] \\ x_1^s \mathrm{e}^{\gamma(\mu)t}\left[(1+\tilde{\varphi}_{21})\sin(t) + \tilde{\varphi}_{22}\cos(t) + o\left(\mathrm{e}^{\gamma(\mu)t}\right)\right] \\ x_3^s \mathrm{e}^{(\gamma(\mu)-\mu_1)t}\left[1+\tilde{\varphi}_{31} + o(\mathrm{e}^{\gamma(\mu)t})\right] \\ \mathrm{e}^{-\beta(\mu)(\tau-t)} \end{pmatrix}. \tag{14}$$

The functions $\tilde{\varphi}_{ij}$ are smooth functions of $(t, x_0, \mu, d_s, \tilde{d}_s, d_u)$ and satisfy $\tilde{\varphi}_{ij} = O(d)$, where $d = \min\{d_s, \tilde{d}_s, d_u\}$. In general, these functions and the o-terms are only C^{k-2}-smooth when the scaled system (13) is C^k [16, 17].

Evaluating $x(t)$ at $t = \tau$, where

$$\tau = -\frac{1}{\beta}\ln(x_4^s), \tag{15}$$

we get the local map Π_{loc},

$$\Pi_{\mathrm{loc}} : \begin{pmatrix} x_1^s \\ x_3^s \\ x_4^s \end{pmatrix} \mapsto \begin{pmatrix} x_1^s (x_4^s)^{\nu(\mu)}\left[(1+\varphi_{11})\cos(\tau) + \varphi_{12}\sin(\tau) + o\left((x_4^s)^{\nu}\right)\right] \\ x_1^s (x_4^s)^{\nu(\mu)}\left[(1+\varphi_{21})\sin(\tau) + \varphi_{22}\cos(\tau) + o\left((x_4^s)^{\nu}\right)\right] \\ x_3^s (x_4^s)^{\nu(\mu)+\mu_1/\beta(\mu)}\left[1+\varphi_{31} + o\left((x_4^s)^{\nu}\right)\right] \end{pmatrix}, \tag{16}$$

where $\nu(\mu)$ is defined by (5) and φ_{ij} are smooth functions of $(x_1^s, x_3^s, x_4^s, \mu)$.

For the global return map $\Pi_{\mathrm{glob}} : \Sigma_u \mapsto \Sigma_s$, we use a general smooth approximation of the flow of (13) from $(0,0,0,1)$ to $(1,0,1,\mu_2)$. Here μ_2 is the aforementioned splitting parameter. It controls the return of the orbit to the critical saddle. For $\mu_2 = 0$ only, we have a primary homoclinic connection.

Thus, the following representation of Π_{glob} can be used

$$\Pi_{\mathrm{glob}} : \begin{pmatrix} x_1^u \\ x_2^u \\ x_3^u \end{pmatrix} \mapsto \begin{pmatrix} 1 \\ 1 \\ \mu_2 \end{pmatrix} + \begin{pmatrix} a_{11}(\mu) & a_{12}(\mu) & a_{13}(\mu) \\ a_{21}(\mu) & a_{22}(\mu) & a_{23}(\mu) \\ a_{31}(\mu) & a_{32}(\mu) & a_{33}(\mu) \end{pmatrix} \begin{pmatrix} x_1^u \\ x_2^u \\ x_3^u \end{pmatrix} + O(\|x^u\|^2), \tag{17}$$

where $x^u = (x_1^u, x_2^u, x_3^u)$. For $A_0 = [a_{ij}(0)]$, we also have $\det(A_0) \neq 0$ which follows from the invertibility of Π_{glob} for μ small enough.

Equations (16) and (17) together give us the full return map $\Pi = \Pi_{\mathrm{glob}} \circ \Pi_{\mathrm{loc}}$. Keeping the dependence of all coefficients on μ implicit, we can write Π as

$$\Pi : \begin{pmatrix} x_1^s \\ x_3^s \\ x_4^s \end{pmatrix} \mapsto \begin{pmatrix} 1 + b_1 x_1^s (x_4^s)^{\nu}\cos\left(-\frac{1}{\beta}\ln x_4^s + \theta_1\right) + b_2 x_3^s (x_4^s)^{\nu+\mu_1/\beta} \\ 1 + b_3 x_1^s (x_4^s)^{\nu}\sin\left(-\frac{1}{\beta}\ln x_4^s + \theta_2\right) + b_4 x_3^s (x_4^s)^{\nu+\mu_1/\beta} \\ \mu_2 + b_5 x_1^s (x_4^s)^{\nu}\sin\left(-\frac{1}{\beta}\ln x_4^s + \theta_3\right) + b_6 x_3^s (x_4^s)^{\nu+\mu_1/\beta} \end{pmatrix} + o(\|x^s\|^{\nu}), \tag{18}$$

where $x^s = (x_1^s, x_3^s, x_4^s)$ and

$$\begin{aligned} \sin\theta_1 &= -\tfrac{a_{12}}{\sqrt{a_{11}^2+a_{12}^2}}, & \cos\theta_2 &= \tfrac{a_{22}}{\sqrt{a_{21}^2+a_{22}^2}}, & \cos\theta_3 &= \tfrac{a_{32}}{\sqrt{a_{31}^2+a_{32}^2}}, \\ b_1 &= \sqrt{a_{11}^2+a_{12}^2}, & b_3 &= \sqrt{a_{21}^2+a_{22}^2}, & b_5 &= \sqrt{a_{31}^2+a_{32}^2}, \\ b_2 &= a_{13}, & b_4 &= a_{23}, & \text{and } b_6 &= a_{33}. \end{aligned} \tag{19}$$

Following [7], we make the smooth invertible transformation $x_4^s \mapsto x_4^s \exp(\theta_3\beta)$ to eliminate θ_3. This gives

$$\Pi : \begin{pmatrix} x_1 \\ x_3 \\ x_4 \end{pmatrix} \mapsto \begin{pmatrix} 1 + \alpha_1 x_1 x_4^{\nu} \cos\left(-\frac{1}{\beta}\ln x_4 + \phi_1\right) + \alpha_2 x_3 x_4^{\nu+\mu_1/\beta} \\ 1 + \alpha_3 x_1 x_4^{\nu} \sin\left(-\frac{1}{\beta}\ln x_4 + \phi_2\right) + \alpha_4 x_3 x_4^{\nu+\mu_1/\beta} \\ \mu_2 + C_1 x_1 x_4^{\nu} \sin\left(-\frac{1}{\beta}\ln x_4\right) + C_2 x_3 x_4^{\nu+\mu_1/\beta} \end{pmatrix} + o(\|x\|^{\nu}), \tag{20}$$

where we have dropped the superscript 's' from the coordinates of $x = (x_1, x_3, x_4)$ for convenience, and where

$$\begin{aligned} \phi_1 &= \theta_1 - \theta_3, & \phi_2 &= \theta_2 - \theta_3, \\ \alpha_1 &= b_1 \exp(\theta_3\beta\nu), & \alpha_2 &= b_2 \exp((\nu + \mu_1/\beta)\theta_3\beta), \\ \alpha_3 &= b_3 \exp(\theta_3\beta\nu), & \alpha_4 &= b_4 \exp((\nu + \mu_1/\beta)\theta_3\beta), \\ C_1 &= b_5 \exp(\theta_3\beta\nu), & C_2 &= b_2 \exp((\nu + \mu_1/\beta)\theta_3\beta). \end{aligned} \tag{21}$$

Observe that α_j and C_k depend on μ and that $C_1 > 0$. Let us denote by α_j^0 and C_j^0 their critical values at $\mu = 0$.

Truncating the $o(\|x\|^{\nu})$ terms in (20) and taking only the critical values of all coefficients, we define

$$G(x, \mu) := \begin{pmatrix} 1 + \alpha_1^0 x_1 x_4^{\nu_0} \cos\left(-\frac{1}{\beta_0}\ln x_4 + \phi_1^0\right) + \alpha_2^0 x_3 x_4^{\nu_0+\mu_1/\beta_0} \\ 1 + \alpha_3^0 x_1 x_4^{\nu_0} \sin\left(-\frac{1}{\beta_0}\ln x_4 + \phi_2^0\right) + \alpha_4^0 x_3 x_4^{\nu_0+\mu_1/\beta_0} \\ \mu_2 + C_1^0 x_1 x_4^{\nu_0} \sin\left(-\frac{1}{\beta_0}\ln x_4\right) + C_2^0 x_3 x_4^{\nu_0+\mu_1/\beta_0} \end{pmatrix}. \tag{22}$$

This map G is the final form of the *3D model return map* that we will use for the numerical analysis ahead.

Now, to analyze periodic orbits close to the homoclinic connection with respect to the critical 3DL saddle, we look for fixed points of the map Π given by (20). These fixed points correspond to periodic orbits in the original ODE system. Bifurcations of these fixed points describe the various local bifurcations of the corresponding periodic orbits.

The fixed point condition for map (20) is

$$\begin{pmatrix} x_1 \\ x_3 \\ x_4 \end{pmatrix} = \begin{pmatrix} 1 + \alpha_1 x_1 x_4^{\nu} \cos\left(-\frac{1}{\beta}\ln x_4 + \phi_1\right) + \alpha_2 x_3 x_4^{\nu+\mu_1/\beta} \\ 1 + \alpha_3 x_1 x_4^{\nu} \sin\left(-\frac{1}{\beta}\ln x_4 + \phi_2\right) + \alpha_4 x_3 x_4^{\nu+\mu_1/\beta} \\ \mu_2 + C_1 x_1 x_4^{\nu} \sin\left(-\frac{1}{\beta}\ln x_4\right) + C_2 x_3 x_4^{\nu+\mu_1/\beta} \end{pmatrix} + o(\|x\|^{\nu}), \tag{23}$$

where all constants α_j and C_k still depend on μ. For non-degeneracy, we require that the real constants C_1 and C_2 are nonzero. We justify this later. The coefficients C_1 and C_2 play the role of *separatrix values* (see [3]).

From (23), we get, using the implicit function theorem, the following expressions for x_1 and x_3:

$$\begin{aligned} x_1 &= 1 + \alpha_1 x_4^{\nu} \cos\left(-\tfrac{1}{\beta}\ln x_4 + \phi_1\right) + \alpha_2 x_4^{\nu+\mu_1/\beta} + o(|x_4|^{\nu}), \\ x_3 &= 1 + \alpha_3 x_4^{\nu} \sin\left(-\tfrac{1}{\beta}\ln x_4 + \phi_2\right) + \alpha_4 x_4^{\nu+\mu_1/\beta} + o(|x_4|^{\nu}), \end{aligned}$$

which gives the condition for x_4

$$x_4 = \mu_2 + C_1 x_4^{\nu} \sin\left(-\frac{1}{\beta}\ln x_4\right) + C_2 x_4^{\nu+\mu_1/\beta} + o(|x_4|^{\nu}), \tag{24}$$

as a 1D fixed point condition. As we are interested in the behavior close to $(1,0,1,0)$ on the cross-section Σ_s, we consider only the leading terms of (24) and introduce the following *scalar model map*:

$$x \mapsto F(x,\mu) := \mu_2 + C_1^0 x^{\nu_0} \sin\left(-\frac{1}{\beta_0}\ln x\right) + C_2^0 x^{\nu_0+\mu_1/\beta_0}. \tag{25}$$

The extra additive term $C_2^0 x^{\nu_0+\mu_1/\beta_0}$ is what makes this map different from the scalar model maps describing the codim 1 saddle-focus case.

If we were to set C_1^0 to zero, then we get the saddle case, where we obtain finitely many fixed points for all values of $\nu_0, \mu_1, \beta_0, \mu_2$ and C_2^0. If we set C_2^0 to zero, we get the codim 1 saddle-focus case.

Thus we assume

(A.5) The homoclinic orbit Γ_0 does not exhibit an additional inclination-flip:

$$C_1^0 C_2^0 \neq 0.$$

3. Analysis of the scalar model map

In this section, we study bifurcations of fixed points of the map (26). To stay close to the 3DL bifurcation, we only work with small values of x and μ. To simplify notations, we rewrite the scalar model map (25) as

$$x \mapsto F(x,\mu) := \mu_2 + C_1 x^{\nu} \sin\left(-\frac{1}{\beta}\ln x\right) + C_2 x^{\nu+\mu_1/\beta}, \tag{26}$$

assuming that ν, β and $C_{1,2}$ are fixed at their critical values.

3.1. Numerical continuation results

Using the continuation package MatContM [18, 19], we obtained many LP and PD bifurcation curves, which form interesting structures. There is strong evidence that there exist infinitely many PD and LP curves in the (μ_1, μ_2)-parameter space. Several such curves can be seen in figure 5. We make the following observations:

(i) The curves exhibit a repetitive behavior: two branches of one LP curve meet to form a horn. The sequence of these horns in the parameter space appears to approach the half axis $\mu_2 = 0 (\mu_1 > 0)$ asymptotically, which is the curve of primary homoclinic orbits. Also, the tips of the horns are always located entirely in either the second or third quadrant of the (μ_1, μ_2)-space.

(ii) The PD and LP curves appear to coincide on visual inspection, and there can exist GPD points in the vicinity of the tip of the LP horn.

(iii) The tip of each LP horn is a cusp point. These cusps always exist for all values of C_1 and C_2 and form a sequence that appears to approach the origin $\mu = 0$.

(iv) Upon closer inspection, we observe that there exists either of the two subtle structures near the top of every LP horn. One is a spring area, where the PD curve loops around the

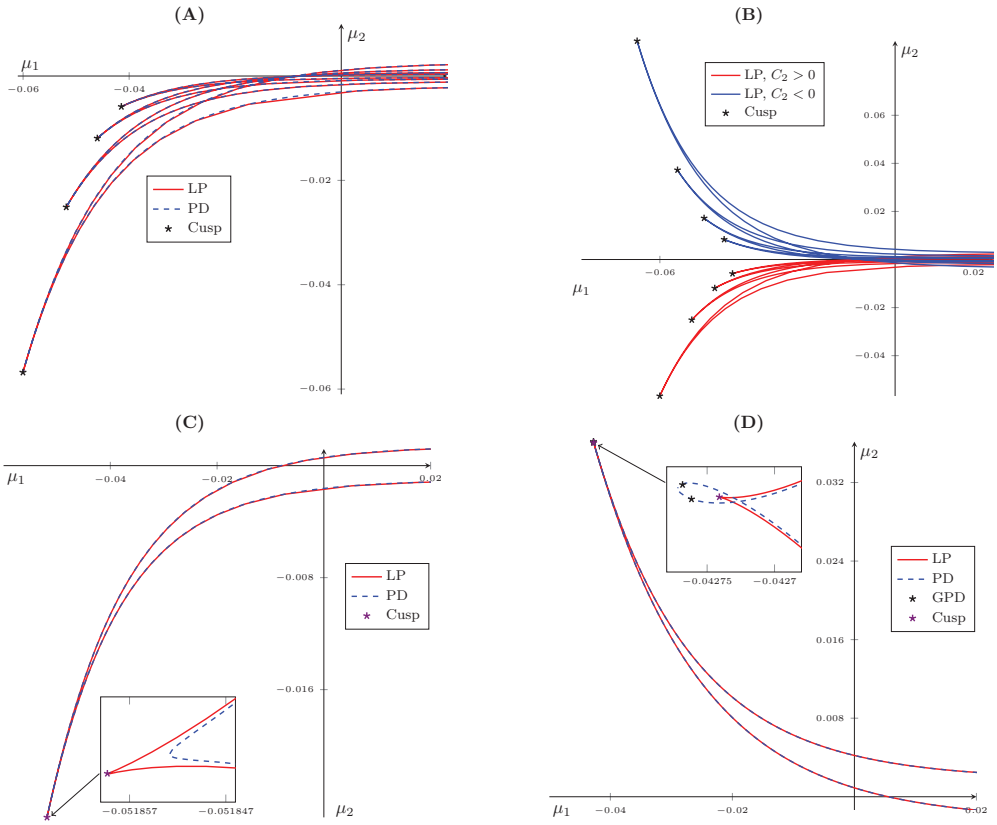

Figure 5. Primary LP and PD bifurcation curves obtained by numerical continuation, for the map (26) for some representative values of C_1 and C_2. We fix $\beta = 0.2$ and $\nu = 0.5$. In panel (A) we plot four pairs of these curves. All of them have the same global structure. There are two types of codimension 2 points that can be found along these curves: cusp (on LP curves) and GPD (along PD curves). In panel (B) we see what happens when we switch the sign of C_2: the horns move from $\mu_2 > 0$ to $\mu_2 < 0$. In panels (C) and (D) we see examples of a PD and LP curve with the saddle area and spring area, respectively (zoomed in). In the insets, μ_2 is scaled for visualization. (A) $C_1 = 1.2$, $C_2 = 0.7$, (B) $C_1 = 1.2$, $C_2 = \pm\, 0.7$, (C) $C_1 = 1.2$, $C_2 = 0.7$ (Saddle area), (D) $C_1 = 0.8$, $C_2 = -1.1$ (Spring area).

cusp point. The other is a saddle area, where the PD curve makes a sharp turn close to the cusp, see the insets in figure 5. The spring area is accompanied by two GPD points along the PD loop. These points are absent in the saddle area. Mira *et al* [13] discuss in detail the spring and saddle areas, including transitions from one case to the other and their genericity.

(v) The global behavior of this set of curves depends on parameters C_1 and C_2. For example, by switching the sign of C_2, the set of curves can be moved from the second to the third quadrant of the μ-space, or vice versa. The presence of saddle or spring areas depends on the parameters C_1 and C_2, but the exact conditions are not clear.

In the sections ahead, we support most of the observations by analytical asymptotics of the LP and PD bifurcation curves of (26).

3.2. Asymptotics

In this section we derive approximate solutions to the LP and PD conditions, and use them to justify numerical observations. As we are interested in solutions close to the 3DL bifurcation point $(\mu_1, \mu_2) = (0, 0)$ we assume that x, μ_1 and μ_2 are sufficiently small. As we investigate only the wild case we restrict ourselves to $\nu < 1$.

3.2.1. LP horns and cusp points. For the scalar model map (26) the fixed point condition is given by

$$\mu_2 + C_1 x^\nu \sin\left(-\frac{1}{\beta}\ln x\right) + C_2 x^{\nu+\mu_1/\beta} - x = 0. \tag{27}$$

Notice that x is a higher-order term compared to x^ν and $x^{\nu+\mu_1/\beta}$ for sufficiently small μ_1. Therefore, studying fixed points is asymptotically equivalent to studying zeros of $F(x, \mu)$. We introduce $\alpha := \min(1, 2\nu)$ and parametrize x using the following relation,

$$-\frac{1}{\beta}\ln x = 2\pi n + \theta, \tag{28}$$

for large $n \in \mathbb{N}$ and $\theta \in (0, 2\pi)$. Thus, (27) becomes

$$\mu_2 + C_1 \mathrm{e}^{-\beta\nu(2\pi n+\theta)} \sin\theta + C_2 \mathrm{e}^{-\beta(\nu+\mu_1/\beta)(2\pi n+\theta)} + O(\mathrm{e}^{-\alpha\beta(2\pi n+\theta)}) = 0. \tag{29}$$

Let us define

$$\Phi(\theta, \mu_1, \mu_2) := \mu_2 + C_1 \mathrm{e}^{-\beta\nu(2\pi n+\theta)} \sin\theta + C_2 \mathrm{e}^{-\beta(\nu+\mu_1/\beta)(2\pi n+\theta)}. \tag{30}$$

Then

$$\Phi_\theta(\theta, \mu_1, \mu_2) = 0,$$

is the extra condition for an asymptotic LP point. Computing the derivative, we get

$$C_1\,(\beta\nu\sin\theta - \cos\theta) + C_2(\beta\nu + \mu_1)\mathrm{e}^{-\mu_1(2\pi n+\theta)} = 0. \tag{31}$$

We now simultaneously solve (27) and (31) to obtain a sequence of functions $\mu_2^{(n)}(\mu_1)$ which describe the sequence of LP horns already observed numerically. Thus, rewriting (31), we have

$$\begin{aligned} \beta\nu\sin\theta - \cos\theta &= -\tfrac{C_2}{C_1}\,(\beta\nu + \mu_1)\,\mathrm{e}^{-\mu_1(2\pi n+\theta)} \\ &= -\tfrac{C_2}{C_1}\,(\beta\nu + \mu_1)\,\mathrm{e}^{-2\pi\mu_1 n}\left[1 - \mu_1\theta + O(\mu_1^2)\right] \\ &= -\tfrac{C_2}{C_1}\mathrm{e}^{-2\pi\mu_1 n}\left[\beta\nu - (1 - \beta\nu\theta)\mu_1 + O(\mu_1^2)\right]. \end{aligned} \tag{32}$$

Collecting trigonometric terms on the left we get

$$\sin(\theta - \phi) = -\frac{1}{\sqrt{1+\beta^2\nu^2}}\frac{C_2}{C_1}\mathrm{e}^{-2\pi\mu_1 n}\left[\beta\nu - (1 - \beta\nu\theta)\mu_1 + O(\mu_1^2)\right], \tag{33}$$

where $\sin\phi = (1+\beta^2\nu^2)^{-1/2}$ and $\phi \in (0, \pi/2)$. Note that for large n and negative μ_1, the corresponding solution θ exists only for small $|\mu_1|$. Let

$$\theta_0^n := \arcsin\left(-\frac{\beta\nu}{\sqrt{1+\beta^2\nu^2}}\frac{C_2}{C_1}\mathrm{e}^{-2\pi\mu_1 n}\right). \tag{34}$$

Then we have two solutions,

$$\begin{aligned}\theta_1 &= \phi + \theta_0^n + 2\pi\delta_{i1} + O(\mu_1),\\ \theta_2 &= \phi + \pi - \theta_0^n + O(\mu_1),\end{aligned} \tag{35}$$

where $i = -\text{sign}(C_2)$ and δ_{ij} is the Kronecker delta.

For each n, we obtain two solutions $\theta = \theta_{1,2}$ given by (35). The corresponding functions $\mu_2^{(n)}(\mu_1)$ follow from (29),

$$\begin{cases}\mu_2^{(n,1)}(\mu_1) = -C_1 \mathrm{e}^{-\beta\nu(2\pi n+\theta_1)}\sin\theta_1 - C_2\mathrm{e}^{-\beta(\nu+\mu_1/\beta)(2\pi n+\theta_1)},\\ \mu_2^{(n,2)}(\mu_1) = -C_1 \mathrm{e}^{-\beta\nu(2\pi n+\theta_2)}\sin\theta_2 - C_2\mathrm{e}^{-\beta(\nu+\mu_1/\beta)(2\pi n+\theta_2)}.\end{cases} \tag{36}$$

On expanding $\sin\theta_1$ and $\sin\theta_2$ we get the expressions for two LP branches forming the nth horn

$$\begin{cases}\mu_2^{(n,1)}(\mu_1) &= -\mathrm{e}^{-\beta\nu(\theta_0^n+\phi+2\pi\delta_{i1})}\frac{\mathrm{e}^{-2\pi\beta\nu n}}{\sqrt{1+\beta^2\nu^2}}\left[C_1\left(1-\frac{\beta^2\nu^2}{1+\beta^2\nu^2}\frac{C_2^2}{C_1^2}\mathrm{e}^{-4\pi\mu_1 n}\right)^{1/2}\right.\\ &\quad\left.+\frac{C_2}{\sqrt{1+\beta^2\nu^2}}\mathrm{e}^{-\mu_1(2\pi n+2\pi\delta_{i1}+\theta_0^n+\phi)}+O(\mu_1)\right],\\ \mu_2^{(n,2)}(\mu_1) &= -\mathrm{e}^{-\beta\nu(\pi-\theta_0^n+\phi)}\frac{\mathrm{e}^{-2\pi\beta\nu n}}{\sqrt{1+\beta^2\nu^2}}\left[-C_1\left(1-\frac{\beta^2\nu^2}{1+\beta^2\nu^2}\frac{C_2^2}{C_1^2}\mathrm{e}^{-4\pi\mu_1 n}\right)^{1/2}\right.\\ &\quad\left.+\frac{C_2}{\sqrt{1+\beta^2\nu^2}}\mathrm{e}^{-\mu_1(2\pi n+\pi-\theta_0^n+\phi)}+O(\mu_1)\right].\end{cases} \tag{37}$$

Upon setting $\mu_2^{(n,j)}$ to zero, we get a sequence $\mu_1^{(n)}\big|_{\mu_2=0}$ of intersections of one of these branches with the axis $\mu_2 = 0$. Thus asymptotically

$$\mu_1^{(n)}\Big|_{\mu_2=0} = \frac{1}{4\pi n}\left[\ln\left(\frac{C_2^2}{C_1^2}\right) + O\left(\frac{1}{n}\right)\right]. \tag{38}$$

For genericity of the LP, we further require that the second derivative $\Phi_{\theta\theta} \neq 0$. Thus, the condition

$$\Phi_{\theta\theta} = 0,$$

determines a cusp point. We solve the following three conditions together

$$\begin{cases}\Phi(\theta,\mu_1,\mu_2) = 0,\\ \Phi_\theta(\theta,\mu_1,\mu_2) = 0,\\ \Phi_{\theta\theta}(\theta,\mu_1,\mu_2) = 0.\end{cases} \tag{39}$$

Differentiating with respect to θ in (33) gives the third equation of (39),

$$\cos(\theta-\phi) + \frac{1}{\sqrt{1+\beta^2\nu^2}}\frac{C_2}{C_1}\mathrm{e}^{-2\pi\mu_1 n}\left[\beta\nu\mu_1 + O(\mu_1^2)\right] = 0. \tag{40}$$

Using (33) and (40) we get

$$\frac{1}{(1+\beta^2\nu^2)}\frac{C_2^2}{C_1^2}\mathrm{e}^{-4\pi\mu_1 n}\left[\beta^2\nu^2 + O(\mu_1)\right] = 1, \tag{41}$$

which gives the value of μ_1 at the cusp point,

$$\mu_1^n = \frac{1}{4\pi n}\left[\ln\left(\frac{\beta^2\nu^2}{(1+\beta^2\nu^2)}\frac{C_2^2}{C_1^2}\right) + O\left(\frac{1}{n}\right)\right]. \tag{42}$$

The corresponding value of μ_2 is obtained from (29). We get

$$\mu_2^n = -\mathrm{e}^{-\beta\nu(2\pi n+\theta_0+\phi)}\frac{\mathrm{sign}(C_2)C_1}{\beta\nu\sqrt{1+\beta^2\nu^2}}a^{-(\theta_0+\phi)/4\pi n} + O\left(\frac{1}{\sqrt{n}}\right), \tag{43}$$

where θ_0 is the value of θ_0^n at the cusp point, that is

$$\theta_0 = \begin{cases}\pi/2, & \text{if } C_2 < 0,\\ 3\pi/2, & \text{if } C_2 > 0,\end{cases} \tag{44}$$

and

$$a = \frac{\beta^2\nu^2}{1+\beta^2\nu^2}\frac{C_2^2}{C_1^2}. \tag{45}$$

Clearly, this cusp point is precisely where the two branches of a horn from (36) meet, i.e. when

$$\sin^2\theta_0^n = 1.$$

3.2.2. PD curves. The formulas derived to describe the LP horns also describe PD bifurcation curves away from the cusp points. Indeed, the asymptotic conditions for PD curves are

$$\begin{cases}\Phi(\theta,\mu_1,\mu_2) = 0,\\ \Phi_\theta(\theta,\mu_1,\mu_2) = 0,\end{cases} \tag{46}$$

which gives the same expressions (35) and (36) to describe PD curves.

3.3. Summarizing lemma for 1D model map

We summarize our findings in the following lemma.

Lemma 3.1. *In a neighborhood of the origin of the (μ_1,μ_2)-plane, the scalar model map (25) has an infinite number of fold curves for fixed points $LP_n^{(1)}$, $n\in\mathbb{N}$, accumulating at the half axis $\mu_2 = 0$ with $\mu_1 \geqslant 0$.*

Each curve resembles a horn with the following asymptotic representation of its two branches:

$$\begin{cases}\mu_2^{(n,1)}(\mu_1) &= -\mathrm{e}^{-\beta_0\nu_0(\theta_0^n+\phi_0+2\pi\delta_{i1})}\frac{\mathrm{e}^{-2\pi\beta_0\nu_0 n}}{\sqrt{1+\beta_0^2\nu_0^2}}\left[C_1^0\left(1-\frac{\beta_0^2\nu_0^2}{1+\beta_0^2\nu_0^2}\frac{(C_2^0)^2}{(C_1^0)^2}\mathrm{e}^{-4\pi\mu_1 n}\right)^{1/2}\right.\\ &\quad\left.+\frac{C_2^0}{\sqrt{1+\beta_0^2\nu_0^2}}\mathrm{e}^{-\mu_1(2\pi n+2\pi\delta_{i1}+\theta_0^n+\phi_0)}+O(\mu_1)\right].\\ \mu_2^{(n,2)}(\mu_1) &= -\mathrm{e}^{-\beta_0\nu_0(\pi-\theta_0^n+\phi_0)}\frac{\mathrm{e}^{-2\pi\beta_0\nu_0 n}}{\sqrt{1+\beta_0^2\nu_0^2}}\left[-C_1^0\left(1-\frac{\beta_0^2\nu_0^2}{1+\beta_0^2\nu_0^2}\frac{(C_2^0)^2}{(C_1^0)^2}\mathrm{e}^{-4\pi\mu_1 n}\right)^{1/2}\right.\\ &\quad\left.+\frac{C_2^0}{\sqrt{1+\beta_0^2\nu_0^2}}\mathrm{e}^{-\mu_1(2\pi n+\pi-\theta_0^n+\phi_0)}+O(\mu_1)\right]\end{cases} \tag{47}$$

where

$$\phi_0 := \arcsin\left(\frac{1}{\sqrt{1+\beta_0^2\nu_0^2}}\right),\quad \theta_0^n := \arcsin\left(-\frac{\beta_0\nu_0}{\sqrt{1+\beta_0^2\nu_0^2}}\frac{C_2^0}{C_1^0}\mathrm{e}^{-2\pi\mu_1 n}\right),$$

and δ_{ij} *is the Kronecker delta where* $i = -\text{sign}(C_2^0)$.

The branches of each $LP_n^{(1)}$ *curve meet at a cusp point* $CP_n^{(1)}$ *with the following asymptotic representation:*

$$CP_n^{(1)} = \begin{pmatrix} \mu_1^n \\ \mu_2^n \end{pmatrix} = \begin{pmatrix} \frac{1}{4\pi n}\left[\ln(a) + O\left(\frac{1}{n}\right)\right] \\ -\mathrm{e}^{-\beta_0\nu_0(2\pi n+\theta_0+\phi_0)}\frac{\text{sign}(C_2^0)C_1^0}{\beta_0\nu_0\sqrt{1+\beta_0^2\nu_0^2}}a^{-(\theta_0+\phi_0)/4\pi n} + O\left(\frac{1}{\sqrt{n}}\right) \end{pmatrix}, \tag{48}$$

where

$$\theta_0 := \begin{cases} \pi/2, & \text{if } C_2^0 < 0, \\ 3\pi/2, & \text{if } C_2^0 > 0, \end{cases}$$

and

$$a := \frac{\beta_0^2\nu_0^2}{1+\beta_0^2\nu_0^2}\frac{(C_2^0)^2}{(C_1^0)^2}\,.$$

Moreover, there exists an infinite number of PD curves $PD_n^{(1)}, n \in \mathbb{N}$, *which have—away from the cusp points* $CP_n^{(1)}$*—the same asymptotic representation as the fold bifurcation curves* $LP_n^{(1)}$. *Depending on* (C_1^0, C_2^0), *the PD curves could either be smooth or have self-intersections developing small loops around the corresponding cusp points.*

Figure 6 illustrates lemma 3.1 by comparing the leading terms of the asymptotic expressions for LP curves with actual LP curves of the 1D model map (25) obtained by accurate numerical continuation.

4. Analyzing the 3D model map

In this section we study the original 3D model map (22) that we restate here for convenience

$$G: \begin{pmatrix} x_1 \\ x_2 \\ x_4 \end{pmatrix} \mapsto \begin{pmatrix} 1 + \alpha_1 x_1 x_4^\nu \cos\left(-\frac{1}{\beta}\ln x_4 + \phi_1\right) + \alpha_2 x_2 x_4^{\nu+\mu_1/\beta} \\ 1 + \alpha_3 x_1 x_4^\nu \sin\left(-\frac{1}{\beta}\ln x_4 + \phi_2\right) + \alpha_4 x_2 x_4^{\nu+\mu_1/\beta} \\ \mu_2 + C_1 x_1 x_4^\nu \sin\left(-\frac{1}{\beta}\ln x_4\right) + C_2 x_2 x_4^{\nu+\mu_1/\beta} \end{pmatrix}. \tag{49}$$

The analysis of fixed points of (49) leads to the same equation (24) for the x_4 coordinate. Thus, all conclusions about the existence and asymptotics of $LP_n^{(1)}$ and $PD_n^{(1)}$ curves, as well as $CP_n^{(1)}$ points in lemma 3.1, remain valid. Indeed, taking into account the $o(|x|^\nu)$-term in (26) does not alter the leading terms in any expression.

4.1. Results of numerical continuation

We look for fixed points of map (49) and their various codim 1 curves. The results are similar to that of the scalar model map, except for higher dimensional codim 2 points that exist only in the 3D model map. In figure 7, we show the PD and LP curves obtained via numerical continuation in μ for a fixed set of parameters:

$$\nu = 0.5, \beta = 0.2, C_1 = 0.8, C_2 = 1.2, \alpha_1 = 0.8, \alpha_2 = 1.3, \alpha_3 = 0.6, \alpha_4 = 1.1, \phi_1 = \phi_2 = \pi/6. \tag{50}$$

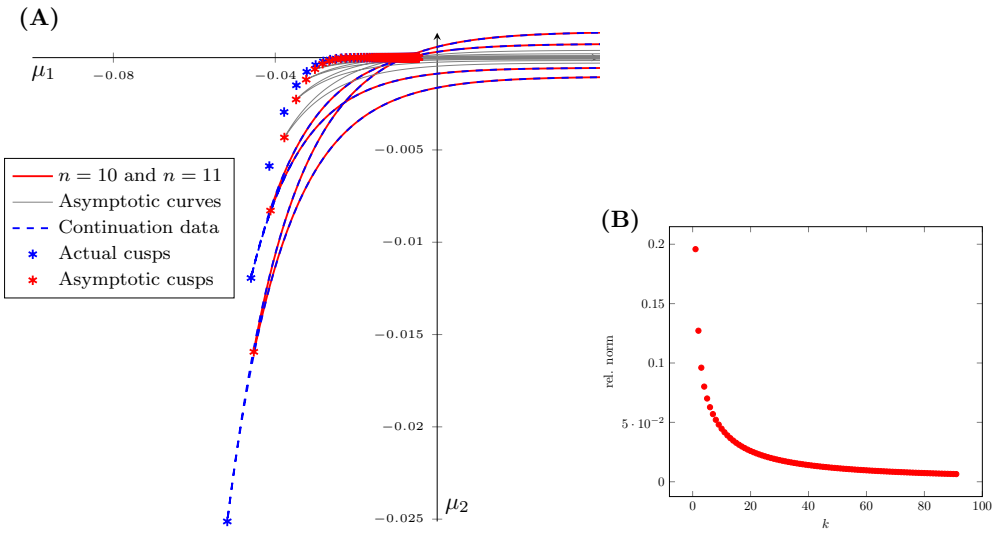

Figure 6. Plots of the truncated asymptotic curves and actual PD/LP curves obtained by numerical continuation. We fix $\beta = 0.2$ and $\nu = 0.5$. In (A) we see how successive asymptotic curves in n approximate the set of PD/LP curves. Here, cusps are obtained by performing Newton iterations to the defining system of the cusp bifurcation with starting points as the asymptotic cusps. In (B), convergence of the asymptotic cusps to the actual cusps is observed. The corresponding values of n in both plots are $n = 10, 11..., 90$. (A) $C_1 = 1.2$, $C_2 = 0.7$, $n = 10, 11, \ldots,$ (B) Relative norm: asymptotic versus actual cusps.

We immediately see similarities with the scalar case. The global structure of these curves is the same as in the scalar case. They form sequences that accumulate on the primary homoclinic curve asymptotically. The LP horns have cusp points and are accompanied by PD curves with/without GPD points (depending on the saddle or spring area). All this is expected as the scalar map is a correct asymptotic representation of the 3D model map.

There are however three main differences with respect to the scalar model map, which can be attributed to the higher dimension of the 3D map:

(i) Spring and saddle areas may occur differently for the 1D and 3D model maps for the same parameter values.
(ii) Between the PD and LP curves, there exist NS curves. The end points of each NS segment are strong resonance points.
(iii) Along the PD, LP and NS curves we observe many higher dimensional codimension 2 points. These points are R1 (resonance 1:1), R2 (resonance 1:2), LPPD (fold-flip), R3 (resonance 1:3), R4 (resonance 1:4).

These points appear to numerically approach the origin $\mu = 0$ (3DL transition). The endpoints of the NS curve are points R1 and R2, as can be seen in figure 7(B). For a detailed discussion on the various codimension 2 points and their local bifurcation diagrams, see [20].

We did not see a significant difference in behavior of the PD/LP curves upon changing the coefficients α_i and ϕ_j. This can be attributed to the effect of the corresponding terms in (49) to the dynamics of x_4. These terms are $o(|x_4|^\nu)$ in the fixed point equation for x_4. In table 1 we present sequences of some of the codimension 2 points found on successive PD/LP curves of

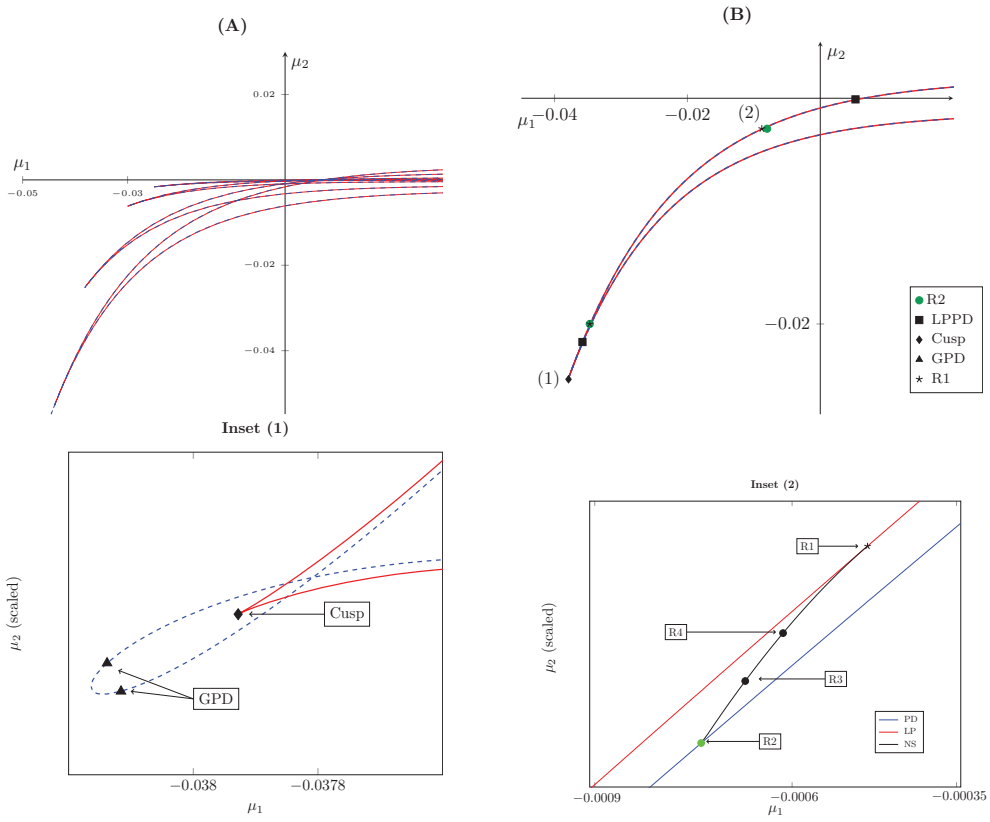

Figure 7. Primary LP (solid red) and PD (dashed blue) curves obtained by numerical continuation for the map (49) with parameters (50). The curves have almost the same global structure as for the 1D map, as can be seen in (A). In (B) one such curve is presented, together with several codim 2 points found along it. In Inset (1) we see the previously described spring area made up by the PD and LP curves. Three codim 2 bifurcation points are observed, two corresponding to the GPD bifurcation and one corresponding to the cusp bifurcation. In Inset (2) we see the interaction between the 1:2 resonance (R2) point on the PD curve and the 1:1 resonance point (R1) on the LP curve, via the primary NS curve (solid black). On this curve we find two more codimension 2 bifurcation points: 1:3 resonance (R3) and 1:4 resonance (R4).

figure 7. These sequences are obtained via detection along PD/LP curves from continuation. GPD and CP points are not reported as they are generally hard to detect along continuations, due to large test function values and absolute gradients. GPDs are approximated in practice by noting where the sign of the corresponding test function changes. Note that codimension 2 points such as R1, R2 and LPPD were observed more than once on a single PD/LP curve. In table 1 we show only one point per curve for each of the different bifurcation points.

For the scalar map we observed that transitions exist between spring and saddle areas. These transitions can be explained by observing the appearance and disappearance of GPD points, as they exist generically on the PD loop in a spring area, and do not exist in the case of a saddle area. In the 3D case too, we numerically observe such transitions. However, when there is a spring (saddle) area in the 3D case, it does not imply that the same structure would exist in the 1D map for the same choice of parameters C_1 and C_2. This is shown in figure 8.

Table 1. Cascades of codimension 2 points numerically obtained during continuation of LP/PD solutions of the 3D map (49). Other parameter values are as in figure 7.

LPPD (1)		R1 (1)		R2 (2)	
μ_1	μ_2	μ_1	μ_2	μ_1	μ_2
$5.9031 \cdot 10^{-3}$	$-2.4503 \cdot 10^{-4}$	$-9.9025 \cdot 10^{-3}$	$-5.1621 \cdot 10^{-3}$	-0.0402	-0.0423
$5.3053 \cdot 10^{-3}$	$-1.3752 \cdot 10^{-4}$	$-8.8301 \cdot 10^{-3}$	$-2.7386 \cdot 10^{-3}$	-0.0347	-0.0200
$4.3915 \cdot 10^{-3}$	$-4.1359 \cdot 10^{-5}$	$-7.2678 \cdot 10^{-3}$	$-7.7386 \cdot 10^{-4}$	-0.0274	$-5.0254 \cdot 10^{-3}$
$3.7375 \cdot 10^{-3}$	$-1.212 \cdot 10^{-5}$	$-6.1795 \cdot 10^{-3}$	$-2.1925 \cdot 10^{-4}$	-0.0227	$-1.3355 \cdot 10^{-3}$
$3.2506 \cdot 10^{-3}$	$-3.5143 \cdot 10^{-6}$	$-5.3758 \cdot 10^{-3}$	$-6.2199 \cdot 10^{-5}$	-0.0195	$-3.6375 \cdot 10^{-4}$
$3.0515 \cdot 10^{-3}$	$-1.8884 \cdot 10^{-6}$	$-5.0477 \cdot 10^{-3}$	$-3.3139 \cdot 10^{-5}$	-0.0182	$-1.9084 \cdot 10^{-4}$
$2.8753 \cdot 10^{-3}$	$-1.0137 \cdot 10^{-6}$	$-4.7574 \cdot 10^{-3}$	$-1.7659 \cdot 10^{-5}$	-0.0160	$-5.288 \cdot 10^{-5}$
$2.7184 \cdot 10^{-3}$	$-5.4376 \cdot 10^{-7}$	$-4.4987 \cdot 10^{-3}$	$-9.4115 \cdot 10^{-6}$	-0.0152	$-2.7905 \cdot 10^{-5}$
$2.3357 \cdot 10^{-3}$	$-8.3651 \cdot 10^{-8}$	$-3.8678 \cdot 10^{-3}$	$-1.4255 \cdot 10^{-6}$	-0.0136	$-7.7986 \cdot 10^{-6}$

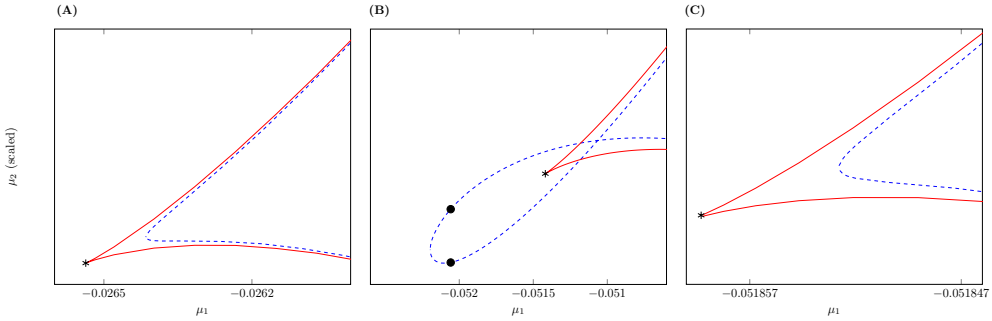

Figure 8. Plots of spring and saddle areas in the scalar map (26) and 3D map (22). We fix $\nu = 0.5, \beta = 0.2, \alpha_1 = 0.8, \alpha_2 = 1.3, \alpha_3 = 0.6, \alpha_4 = 1.1$ and $\phi_1 = \phi_2 = \pi/6$. In all plots μ_2 is scaled for convenience. In (A) we see that there exists a saddle area in the 3D case, where GPD points are absent. (B) and (C) are plotted for the same value of C_1 and C_2, but with respect to the 3D map (22) and 1D map (26), respectively. We see that the existence of the spring area in the 3D map does not imply the existence of the same in the 1D map. Other parameters are fixed as in figure 7. (A) $C_1 = 0.5$, $C_2 = 1.1$, (B) $C_1 = 1.2$, $C_2 = 0.7$, (C) 1D map: $C_1 = 1.2$, $C_2 = 0.7$.

4.2. Secondary homoclinic orbits

In this section we analyze a particular type of homoclinic orbit, i.e. *secondary* homoclinic orbits, which—after leaving the saddle along the unstable manifold—make two global excursions before returning to the saddle.

We look at the existence of these homoclinic orbits close to the primary homoclinic orbit in (2), upon perturbing parameters μ_1 and μ_2. The existence of the orbits is a codim 1 situation and corresponds to a curve in the (μ_1, μ_2)-plane. As before, we look for these curves in the wild case, where $\nu < 1$. In the tame case $\nu > 1$, they do not exist.

Consider figure 9. The secondary homoclinic orbit Γ_1 in the scaled ODE (13) leaves the point $y_u = (0, 0, 0, 1) \in \Sigma_u$ along the unstable manifold and crosses Σ_s at $x = (x_1^s, 0, x_3^s, \mu_2)$. From this point, the orbit departs again and this time returns along the stable manifold, thus approaching the origin. The orbit then crosses Σ_s at $y_s = (1,0,1,0)$. Using the 3D model map G defined by (49), the condition is

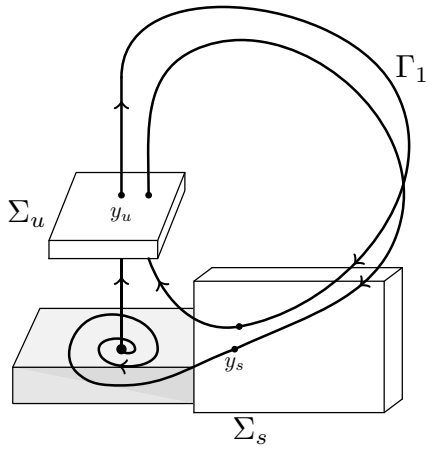

Figure 9. Poincaré map for the secondary homoclinic solution Γ_1. Upon leaving y_u along the unstable manifold, the corresponding orbit makes two global excursions and returns to the origin.

$$G\begin{pmatrix}1\\1\\\mu_2\end{pmatrix} = \begin{pmatrix}1\\1\\0\end{pmatrix}, \tag{51}$$

which implies

$$\mu_2 + C_1\mu_2^{\nu}\sin\left(-\frac{1}{\beta}\ln\mu_2\right) + C_2\mu_2^{\nu+\mu_1/\beta} = 0. \tag{52}$$

Let us define

$$H(\mu) := \mu_2 + C_1\mu_2^{\nu}\sin\left(-\frac{1}{\beta}\ln\mu_2\right) + C_2\mu_2^{\nu+\mu_1/\beta}. \tag{53}$$

Note that here μ_2 must be positive. The shape of $H(\mu) = 0$ is similar to the curve $F(x, \mu) = 0$ (from (26)). For positive μ_1, it is possible to obtain infinitely many solutions of (52) for μ_2 sufficiently small. That is not the case when $\mu_1 < 0$, as there are only finitely many or no non-trivial solutions for μ_2 sufficiently small.

In figure 10 the non-trivial solutions are continued with respect to the parameters μ_1 and μ_2 for two different sets of values of C_1 and C_2. We observe three things:

(i) There are secondary homoclinic curves which form *horizontal parabolas* and these parabolas approach the primary homoclinic curve $\mu_2 = 0$ asymptotically.
(ii) These parabolas possess *turning* points where the two upper and lower secondary homoclinic branches merge. The sequence of turning points obtained from successive parabolas appears to approach the origin asymptotically.
(iii) For different values of C_1 and C_2, the sequence of turning points is located strictly either in the first or second quadrant.

4.3. Asymptotics of secondary homoclinics

The observations above can be explained to some extent by asymptotic expressions for the parabolas and the corresponding turning points.

Noticing $\mu_2 > 0$, let

$$-\frac{1}{\beta}\ln\mu_2 = 2\pi m + \theta, \tag{54}$$

for large $m \in \mathbb{N}$ and $\theta \in (0, 2\pi)$. On dividing both sides by $\mu_2^\nu \neq 0$ and using the above parameterization for μ_2, (52) becomes

$$\mathrm{e}^{-\beta(1-\nu)(2\pi m+\theta)} + C_1\sin\theta + C_2\mathrm{e}^{-\mu_1(2\pi m+\theta)} = 0. \tag{55}$$

On simplifying, we get

$$\sin\theta = -\frac{C_2}{C_1}\mathrm{e}^{-2\pi\mu_1 m}(1-\mu_1\theta + O(\mu_1^2)) + O(\mathrm{e}^{-\alpha m}), \tag{56}$$

where $\alpha = 2\pi\beta(1-\nu)$. For large m and negative μ_1, a solution θ exists only for small $|\mu_1|$. Thus we get two solutions θ from (56),

$$\begin{aligned}\theta_1 &= \theta_0^m + 2\pi\delta_{i1} + O(1/m),\\ \theta_2 &= \pi - \theta_0^m + O(1/m),\end{aligned} \tag{57}$$

where

$$\theta_0^m := \arcsin\left(-\frac{C_2}{C_1}\mathrm{e}^{-2\pi\mu_1 m}\right),$$

the index $i = -\mathrm{sign}(C_2)$ and δ_{ij} is the Kronecker delta. Thus the expressions for the two 'half-parabolas' are

$$\begin{cases}\mu_2^{(m,1)} &= \mathrm{e}^{-\beta(2\pi m+\theta_0^m+2\pi\delta_{i1})}(1+O(1/m)),\\ \mu_2^{(m,2)} &= \mathrm{e}^{-\beta(2\pi m+\pi-\theta_0^m)}(1+O(1/m)).\end{cases} \tag{58}$$

Taking derivative with respect to θ in (56) gives

$$\cos\theta = \frac{C_2}{C_1}\mathrm{e}^{-2\pi\mu_1 m}(\mu_1 + O(\mu_1^2)) + O(\mathrm{e}^{-\alpha m}). \tag{59}$$

Solving (56) and (59) together gives the condition for the turning points. Using the two conditions gives

$$\frac{C_2^2}{C_1^2}\mathrm{e}^{-4\pi\mu_1 m}(1+O(\mu_1)) + O(\mathrm{e}^{-\alpha m}) = 1. \tag{60}$$

From this we get μ_1,

$$\mu_1 = \frac{1}{4\pi m}\left[\ln\left(\frac{C_2^2}{C_1^2}\right) + O\left(\frac{1}{m}\right)\right], \tag{61}$$

which also follows from the condition

$$\sin^2\theta = 1. \tag{62}$$

Thus the sequence of turning points is given by

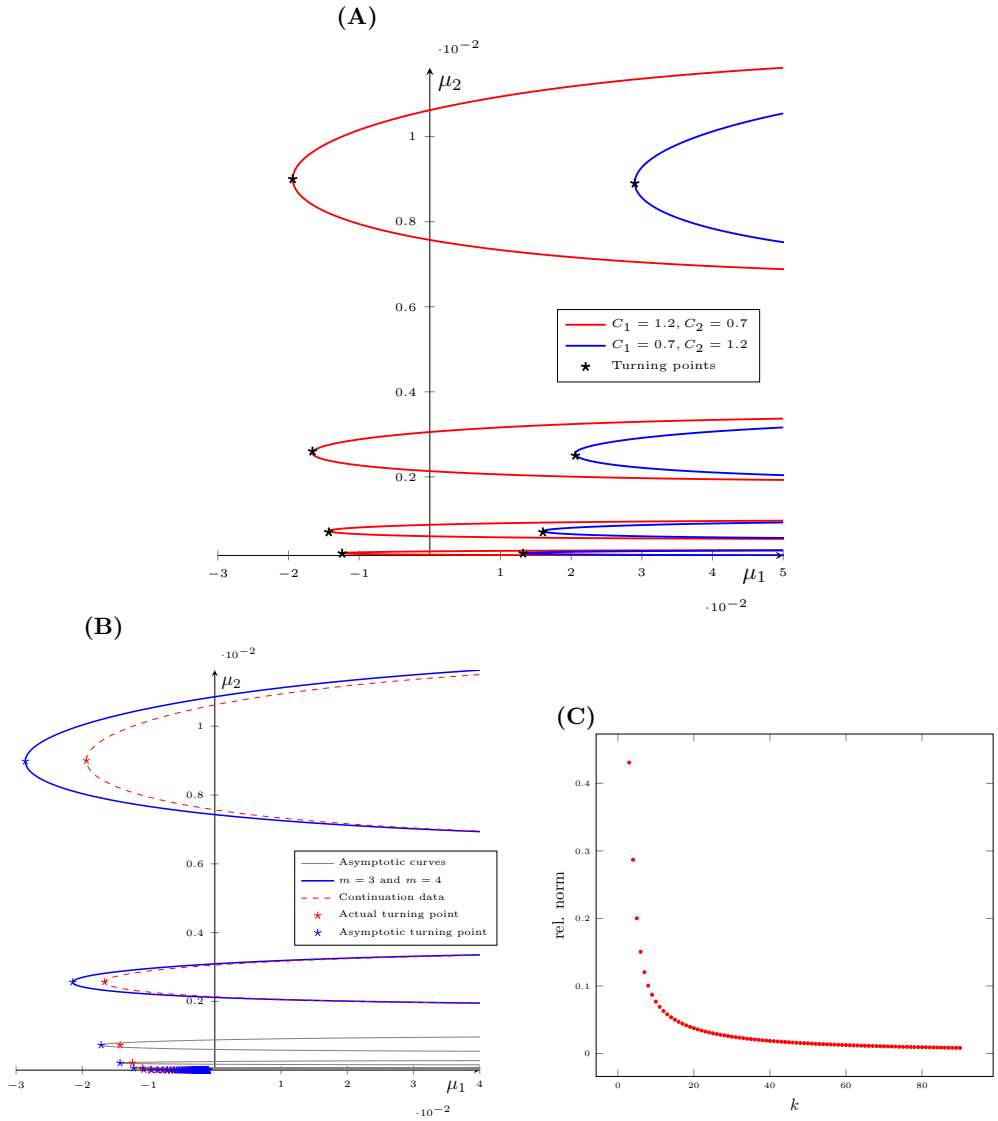

Figure 10. Solutions of (52) in (μ_1, μ_2)-space. We fix $\beta = 0.2$ and $\nu = 0.5$. In (A), parabolas are obtained via continuation in MatCont, for two sets of parameter values. The turning points (in black) are computed with high accuracy by Newton iterations. In (B), the computed curves are plotted together with asymptotic curves defined by the leading terms in (66). In (C), we plot relative norm differences between asymptotic and numerically computed turning points. (A) Continuations: $m = 3, 4...6$, (B) $C_1 = 1.2, C_2 = 0.7$, $m = 3, 4..., 90$, (C) Convergence: $C_1 = 1.2$, $C_2 = 0.7$.

$$\begin{pmatrix} \mu_1^{(m)} \\ \mu_2^{(m)} \end{pmatrix} = \begin{pmatrix} \frac{1}{(4\pi m)} \left(\ln\left(\frac{C_2^2}{C_1^2}\right) + O\left(\frac{1}{m}\right)\right) \\ \mathrm{e}^{-\beta(2\pi m + \theta_0)} \left(1 + O\left(\frac{1}{m}\right)\right) \end{pmatrix}, \tag{63}$$

where

$$\theta_0 = \begin{cases} \pi/2, & \text{if } C_2 < 0, \\ 3\pi/2, & \text{if } C_2 > 0. \end{cases} \tag{64}$$

We summarize the results in the following lemma.

Lemma 4.1. *For the 3D model map G defined by (22), the condition*

$$G\begin{pmatrix} 1 \\ 1 \\ \mu_2 \end{pmatrix} = \begin{pmatrix} 1 \\ 1 \\ 0 \end{pmatrix} \tag{65}$$

defines in a neighborhood of the origin of the (μ_1, μ_2)-plane, an infinite sequence of parabolas $\mathrm{Hom}_m^{(2)}$, $m \in \mathbb{N}$, *that accumulate onto the half axis $\mu_2 = 0$ with $\mu_1 \geqslant 0$. Each parabola is formed by two branches with the following asymptotic representation:*

$$\begin{cases} \mu_2^{(m,1)} = \mathrm{e}^{-\beta_0(2\pi m + \theta_0^m + 2\pi\delta_{i1})}\left(1 + O\left(\frac{1}{m}\right)\right), \\ \mu_2^{(m,2)} = \mathrm{e}^{-\beta_0(2\pi m + \pi - \theta_0^m)}\left(1 + O\left(\frac{1}{m}\right)\right), \end{cases} \tag{66}$$

where

$$\theta_0^m := \arcsin\left(-\frac{C_2^0}{C_1^0}\mathrm{e}^{-2\pi\mu_1 m}\right).$$

These branches meet at a sequence of turning points $T_m^{(2)}$, which converges to the origin of the (μ_1, μ_2)-plane and is given by

$$T_m^{(2)} = \begin{pmatrix} \mu_1^{(m)} \\ \mu_2^{(m)} \end{pmatrix} = \begin{pmatrix} \frac{1}{(4\pi m)}\left(\ln\left[\frac{(C_2^0)^2}{(C_1^0)^2}\right] + O\left(\frac{1}{m}\right)\right) \\ \mathrm{e}^{-\beta_0(\pi m + \theta_0)}\left(1 + O\left(\frac{1}{m}\right)\right) \end{pmatrix}, \tag{67}$$

where

$$\theta_0 = \begin{cases} \pi/2, & \text{if } C_2 < 0, \\ 3\pi/2, & \text{if } C_2 > 0. \end{cases} \tag{68}$$

5. Interpretation of the original ODE system

Let us consider the original 4D system (2) in the (u, v)-coordinates (7) near the equilibrium, the geometric construction in figure 4 and the full 3D map Π defined by (20).

Fixed points of this map Π in Σ_s correspond to periodic orbits, thus PD and fold bifurcations of these fixed points of this map correspond to the same bifurcations of periodic orbits in the original ODE system.

The second iterate of the map (20), for $\mu_2 > 0$, defines an orbit in the original system (2) which makes an extra global excursion before returning to Σ_u. Starting at a point in the unstable 1D manifold of the equilibrium and letting the third component of the image go to zero, implies that we consider an orbit of the ODE that departs along the unstable manifold and returns along the stable manifold back to the saddle. This orbit is therefore a secondary homoclinic orbit near the primary one.

Using lemmas 3.1 and 4.1 we are now able to formulate our main results in terms of the original 4D ODE near the wild 3DL homoclinic transition. It follows from the fact that taking into account the $o(\|x\|^{\nu})$-term in (20) does not alter the leading terms in all expressions, which further implies that the given asymptotics are the same for the truncated map (49) and full 3D return map (20).

Theorem 5.1. *Consider a smooth 4D ODE system depending on two parameters*

$$\dot{x} = f(x, \alpha),\ x \in \mathbb{R}^4,\ \alpha \in \mathbb{R}^2. \tag{69}$$

Suppose that at $\alpha = 0$ *the system* (69) *satisfies the following assumptions:*

(A.1) *The eigenvalues of the linearization at the critical 3DL equilibrium* $x = 0$ *are*

$$\delta_0, \delta_0 \pm \mathrm{i}\omega_0 \text{ and } \epsilon_0,$$

where $\delta_0 < 0, \omega_0 > 0$, $\epsilon_0 > 0$ *and* $\sigma_0 = \delta_0 + \epsilon_0 > 0$.

(A.2) *There exists a primary homoclinic orbit* Γ_0 *to this 3DL equilibrium.*

Then, in addition to the primary homoclinic curve $\mathrm{Hom}^{(1)}$*, the bifurcation set of* (69) *in a neighborhood of* $\alpha = 0$ *generically contains the following elements:*

(i) *An infinite number of fold bifurcation curves* $LP_n^{(1)}, n \in \mathbb{N}$*, along which limit cycles with multiplier* $+1$ *exist making one global excursion and a number of small turns near the equilibrium. These curves accumulate in the saddle-focus part of the primary homoclinic curve. Each curve resembles a horn consisting of two branches that meet at a cusp point* $CP_n^{(1)}$*. The sequence of cusp points converges to* $\alpha = 0$.

(ii) *An infinite number of period-doubling bifurcation curves* $PD_n^{(1)}, n \in \mathbb{N}$*, along which limit cycles with multiplier* -1 *exist making one global excursion and a number of small turns near the equilibrium. Away from the cusp points* $CP_n^{(1)}$*, these PD curves have the same asymptotic properties as the fold bifurcation curves* $LP_n^{(1)}$*. These PD curves could either be smooth or have self-intersections developing small loops around the corresponding cusp points.*

(iii) *An infinite number of secondary homoclinic curves* $\mathrm{Hom}_m^{(2)}, m \in \mathbb{N}$*, along which the equilibrium has homoclinic orbits making two global excursions and a number of turns near the equilibrium after the first global excursion. These curves also accumulate in the saddle-focus part of the primary homoclinic curve. Each curve resembles a parabola and the sequence of turning points converges to* $\alpha = 0$.

The genericity mentioned in the theorem means the nondegeneracy conditions **(A.3)**–**(A.5)**. Part (i) of theorem 5.1 is illustrated in figure 11. Notice that $LP_n^{(1)}$ curves can intersect the primary homoclinic branch $\mathrm{Hom}^{(1)}$ either at saddle points (figure 11(a)) or at saddle-focus points (figure 11(b)). In terms of the 1D (or 3D) model map these cases correspond to $C_1^0 > |C_2^0|$ or $0 < C_1^0 < |C_2^0|$, respectively. See equation (38).

Part (iii) of theorem 5.1 is illustrated in figure 12. Notice that the turning points of the secondary homoclinic curves $\mathrm{Hom}_m^{(2)}$ approach the 3DL transition point on $\mathrm{Hom}^{(1)}$ either along its saddle part (figure 12(a)) or its saddle-focus part (figure 12(b)). Note that in case (a) we have an infinite sequence of pairs of secondary 3DL transitions accumulating at the primary 3DL transition. In terms of the 2D (or 3D) model map these cases also correspond to $C_1^0 > |C_2^0|$ or $C_1^0 < |C_2^0|$, respectively. See equation (61).

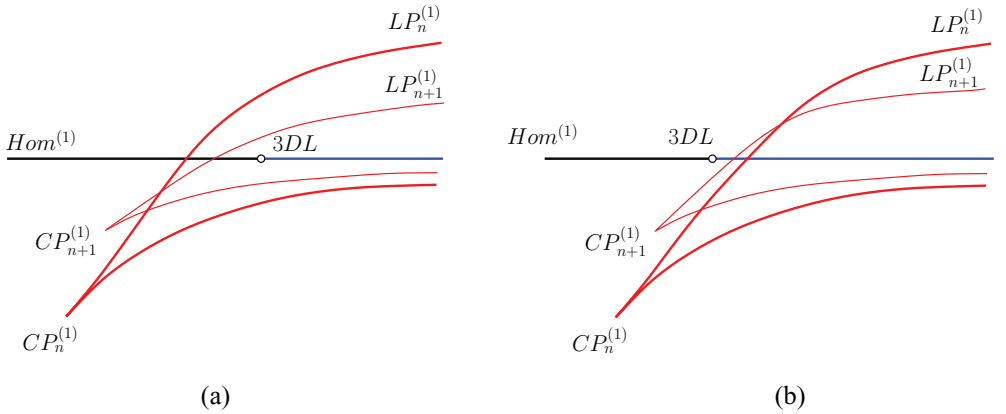

Figure 11. A sketch of two consecutive LP horns from theorem 5.1. The saddle-focus part of $\mathrm{Hom}^{(1)}$ branch is drawn in blue. The difference between cases (a) and (b) is explained in the text.

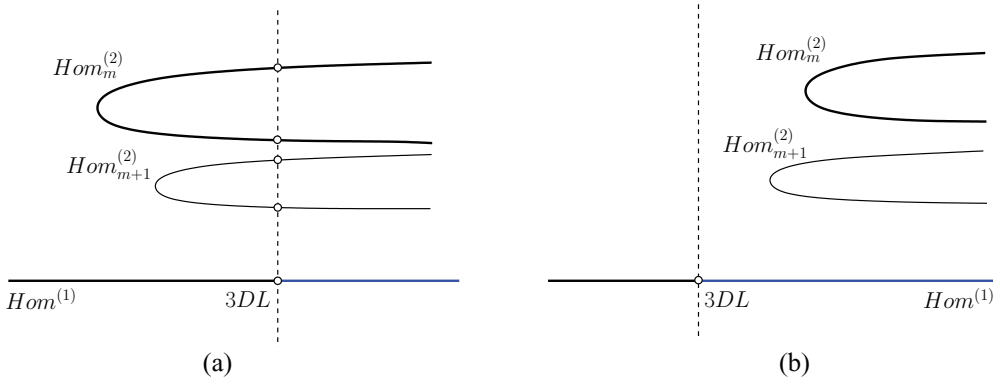

Figure 12. A sketch of two consecutive secondary homoclinic curves from theorem 5.1. The saddle-focus part of $\mathrm{Hom}^{(1)}$ branch is drawn in blue. The difference between cases (a) and (b) is explained in the text. The vertical dashed line indicates the saddle to saddle-focus transition. In case (a) the points where the secondary homoclinic curves intersect the dashed line correspond to secondary 3DL transitions.

Our numerical analysis of the truncated model 3D map (22) also reveals NS curves in very small domains between the PD and LP curves. These curves correspond to *torus* bifurcation of cycles in the ODE system and do not exist for all combinations of (C_1^0, C_2^0). The end points of the NS segment are strong resonance points. There are other codimension 2 points, i.e. GPDs and LPPDs. All these points will also be present in the generic ODE system and should form sequences that converge to the 3DL transition point.

6. Examples

In this section we study the presence of the 3DL transition in two 4D ODE models.

6.1. Neural field model

In [12], a 3DL transition was observed in a traveling wave system for a neural field equation. The corresponding ODE system is

$$\begin{cases} \dot{u} &= \frac{-u+\psi-a}{c}, \\ \dot{\phi} &= \phi, \\ \dot{\psi} &= \psi - f(u), \\ \dot{a} &= \frac{\kappa u - a}{c\tau}, \end{cases} \tag{70}$$

where $f(u) = (1 + \exp(\beta(u-\theta)))^{-1}$. The parameters $\beta = 20, \tau = 4.4, \theta = 0.3$ are fixed and κ, c are varied. The adaptation strength κ influences which wavespeeds c are admissible. Figure 13(a) shows a part of the bifurcation diagram where the homoclinic orbit corresponding to a traveling wave is recomputed using MatCont [21, 22]. The upper part of this curve involves stable waves. On the homoclinic orbit we have detected two codim 2 bifurcation points. The first is the 3DL point at $(\kappa, c) \approx (0.7413, 0.4213)$, while a neutral saddle (Wild-Tame, WT) occurs at $(\kappa, c) \approx (0.7415, 0.5232)$. The real part of the eigenvalues along the branch is shown in figure 13(b). At the 3DL point we have eigenvalues $\lambda_1 = 0.9847, \lambda_2 = -1.2999, \lambda_{3,4} = -1.2999 \pm 0.058\mathrm{i}$. So this concerns the *tame* case ($\nu_0 > 1$), while the saddle-focus switches from tame to wild at the neutral saddle (WT). Next, we were able to locate two limit point of cycle horns with corresponding cusps (using 120 mesh points with default tolerances). As predicted, we observe only finitely many horns as this example exhibits the tame case. Note that CP^2 corresponds to a cycle with higher period than CP^1, and is further away from 3DL.

The significance of the two codim 2 points is as follows. As we start from $c = 0.4$ and increase c, we have a saddle-homoclinic orbit and move past the 3DL point. We then have a tame saddle-focus homoclinic orbit. For nearby parameters, there are only finitely many periodic orbits. For the traveling waves, this implies the existence of a finite number of periodic pulses (*wave trains*), see [12] for more details. The additional wave trains appear from the limit point of cycle bifurcations. Beyond the WT point, there are infinitely many such waves.

6.2. Lorenz–Stenflo model

As an example of a wild 3DL transition, we study the Lorenz–Stenflo equations. These equations are a generalization of the well-known Lorenz equations [23], that describe low-frequency, short-wavelength acoustic gravity perturbations in the atmosphere with additional dependence on the earth's rotation. The Lorenz–Stenflo equations are as follows:

$$\begin{cases} \dot{x} &= \sigma(y-x) + su, \\ \dot{y} &= rx - xz - y, \\ \dot{z} &= xy - bz, \\ \dot{u} &= -x - \sigma u, \end{cases} \tag{71}$$

where σ is the Prandtl number, r is a generalized Rayleigh parameter, b is a positive parameter and s is a new parameter dependent on the Earth's rotation [24]. Setting $s = 0$ reduces the first three equations in (73) back to the original Lorenz model. The system (71) demonstrates chaotic dynamics and has a very complicated bifurcation diagram [25–27].

System (71) possesses the $\mathbb{Z}_2$-symmetry

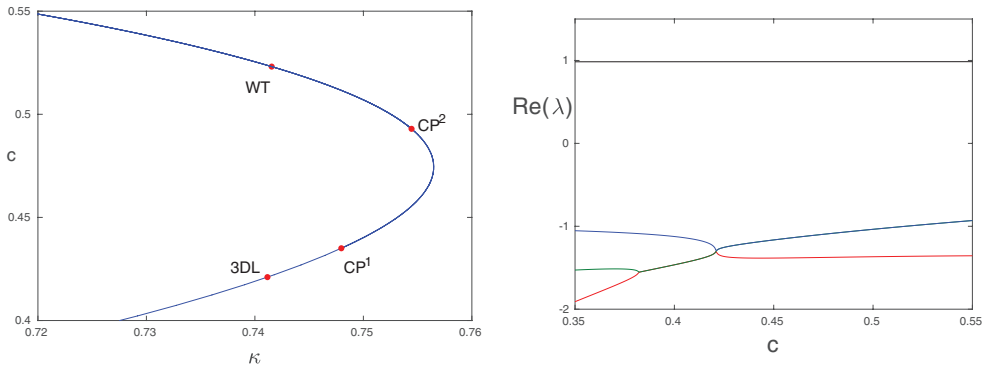

Figure 13. Bifurcation diagram of system (70). (a) The homoclinic bifurcation curve exhibits two codim 2 points, 3DL and WT. Near the homoclinic bifurcation curve there are two more folds of cycle bifurcation curves. They are too close to the homoclinic to be resolved, but both fold curves exhibit a cusp bifurcation $\mathsf{CP}^{1,2}$. (b) Real part of eigenvalues of the saddle on the homoclinic bifurcation curve. At $c = 0.4213$, the three stable eigenvalues are distinct but have equal real parts. At $c = 0.5232$, the saddle quantity vanishes. (a) Partial bifurcation diagram. (b) Real part of eigenvalues.

$$(x, y, z, u) \mapsto (-x, -y, z, -u),$$

and has one or three equilibria (the trivial equilibrium exists always). The system exhibits a wild 3DL transition of the primary homoclinic orbit to the trivial equilibrium at parameter values

$$\sigma = 2,\ s = 203.479\,75,\ r = 126.435\,27,\ b = 6, \tag{72}$$

for which the eigenvalues are $\delta_0 \pm \mathrm{i}\omega_0$, δ_0 and ϵ_0 with $\delta_0 = -6$, $\omega_0 \approx 2.5708$, and $\epsilon_0 \approx 7$, so that $\nu_0 < 1$ indeed. However, the corresponding PD and LP curves are difficult to resolve due to highly contractive properties close to the transition, caused by large real parts of the eigenvalues at the trivial equilibrium. Moreover, its bifurcation diagram will include additional bifurcation curves, e.g. related to (symmetric) cycles and heteroclinic orbits.

To overcome this, we perturb the system to get

$$\begin{cases} \dot{x} &= \sigma(y - x) + su, \\ \dot{y} &= rx - xz - y + \boldsymbol{\epsilon_1 z}, \\ \dot{z} &= xy - bz, \\ \dot{u} &= -x - \sigma u + \boldsymbol{\epsilon_2 y}, \end{cases} \tag{73}$$

where the bold expressions are perturbation terms. This system is not $\mathbb{Z}_2$-symmetric anymore, but still has a trivial equilibrium for all parameter values. We are not aware of any physical interpretation of the added terms.

The trivial equilibrium has homoclinic orbits, and in figure 14, we see a wild 3DL transition along the primary homoclinic curve (black) in the perturbed Lorenz–Stenflo system (73) with

$$\sigma = 0.1,\ s = 33,\ \epsilon_1 = 0.1,\ \epsilon_2 = 0.3. \tag{74}$$

The 3DL transition point is located at

$$(r, b) \approx (15.302\,531, 1.9884).$$

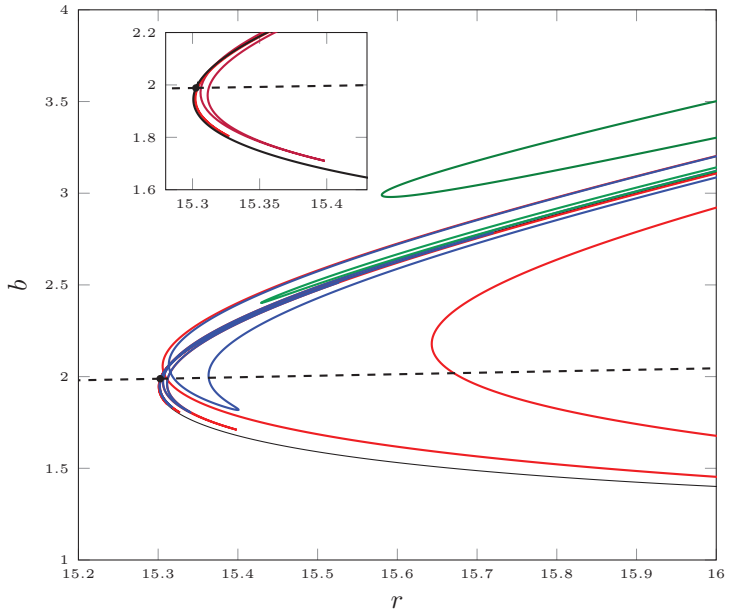

Figure 14. Bifurcation curves near a wild 3DL transition in the (b, r)-plane: cyclic folds (red), PDs (blue), primary homoclinic (black), 3DL equilibrium transition (dashed black) and secondary homoclinics (green). For other parameter values, see (74).

The corresponding eigenvalues are $\delta_0 \pm \mathrm{i}\omega_0, \delta_0$ and ϵ_0 with $\delta_0 \approx -1.9884, \omega_0 \approx 6.2265, \epsilon_0 \approx 2.7769$, so that $\nu_0 < 1$ as well.

We clearly see PD (blue) and LP (red) curves accumulating on the primary homoclinic curve according to the theory. The PD curve within each horn forms a saddle area. The secondary homoclinic curves (green) form parabolas on one side of the primary homoclinic curve as expected. The curve of trivial equilibria with a 3D stable eigenspace is shown as a dashed line. The cusp points on each LP horn form a sequence, and asymptotically approach the 3DL point at the intersection of the black curve with the dashed line. The inset shows only the LP horns. For this model the bifurcation curves have been computed using MatCont [21], also based on [22, 28]. There are, however, no stable chaotic dynamics in the parameter range of figure 14.

We have also computed *kneading indices* [29, 30] to characterize the nature of attractors in parameter space in more detail. At each point in the parameter space, an orbit is computed starting from a phase point near the trivial equilibrium shifted in the unstable direction with x negative. Next, the number of extrema in the x-variable are indexed as follows. For the ith extremum at time t_i we have

$$c_i = \begin{cases} 1, & \text{if } x(t_i) < 0, \\ 0, & \text{if } x(t_i) > 0. \end{cases} \tag{75}$$

Next we compute the finite approximation of the *kneading index*,

$$K = \sum_{i=1}^{N} c_i q^i, \tag{76}$$

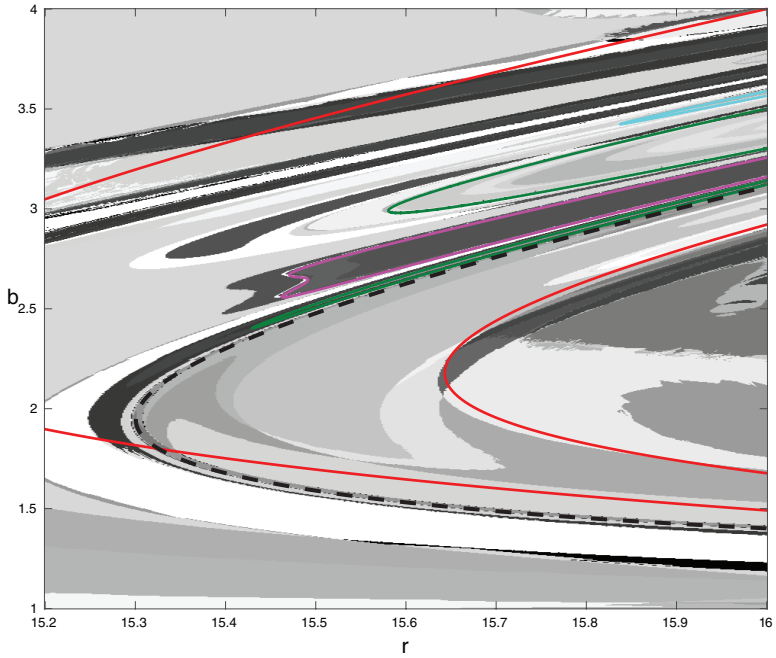

Figure 15. Kneading indices for the perturbed Lorenz–Stenflo model (73) in the (b, r)-plane for fixed parameters (74). Color codes in gray indicate domains with the same kneading index. The following bifurcation curves computed in MatCont are overlaid: primary homoclinic (black, dashed), secondary homoclinic (green), tertiary homoclinic (pink), quadruple homoclinic (blue) and cyclic fold (red).

where q is chosen to be less than 1 and N is finite. The value of K itself bears no meaning, but a change in index may quantify the following events: either there is a homoclinic bifurcation, or one of the extrema of the time series passes zero. The latter is not a bifurcation as there is no structural change in the dynamics. It is difficult, however, to eliminate such false bifurcations automatically. In figure 15 we overlay homoclinic bifurcation curves to find agreement between changes in the kneading index and homoclinic bifurcation curves. The changes in color indicate where one may find a homoclinic bifurcation. Kneading indices are typically used for symmetric systems which allow a clear threshold to set c_i, but as a first inventory of homoclinic bifurcations prove rather useful here, e.g. the double and triple homoclinic bifurcation curves.

7. Discussion

We have studied bifurcation diagrams of 4D two-parameter ODEs having at some critical parameter values a homoclinic orbit to a hyperbolic equilibrium with one simple unstable eigenvalue and three simple stable eigenvalues (one real and one complex-conjugate pair). We demonstrated that this phenomenon occurs in two 4D ODE systems appearing in applications. We focused on the case where a transition from a saddle homoclinic orbit to Shilnikov's wild saddle-focus homoclinic orbit takes place at the critical parameter values. Similar to the 3D Belyakov's saddle to wild saddle-focus homoclinic transition, we found infinite sequences of codim 1 bifurcations curves related to limit cycles, i.e. folds and PDs, and secondary homoclinic

orbits accumulating on the primary (wild) saddle-focus homoclinic branch. However, there is a striking difference between these two cases. While in the standard Belyakov case all bifurcation curves approach the codim 2 point in the parameter plane tangentially to the saddle-focus homoclinic curve (having actually tangency of infinite order) and form bunches, in the considered 3DL case none of them emanate from the codim 2 point. Instead, they form sequences of horns with cusps and other codim 2 bifurcation points, or parabolas. The sequences of codim 2 points and parabola tips indeed converge to the studied homoclinic 3DL point. In a sense, the bifurcation diagram for the considered 3DL transition more resembles another codim 2 homoclinic bifurcation studied by Belyakov: a transition from tame to wild saddle-focus homoclinic orbit in 3D ODEs, when the saddle quantity vanishes [31]. In that case, fold bifurcation curves for cycles also have cusp points accumulating at the transition point, while the secondary homoclinic curves look like parabolas with tips tending to the transition point. The exact source of this similarity remains a mystery but might be related to the simplicity of all eigenvalues in both cases.

One can employ the C^1 linearization theorem by Belitskii [1, 32] to get the C^1 equivalence of the flow generated by (2) to that corresponding to its linear part, near the equilibrium $O = (0, 0, 0, 0)$

$$\begin{cases} \dot{x_1} = \gamma(\mu)x_1 - x_2, \\ \dot{x_2} = x_1 + \gamma(\mu)x_2, \\ \dot{x_3} = (\gamma(\mu) - \mu_1)\, x_3, \\ \dot{x_4} = \beta(\mu)x_4. \end{cases} \tag{77}$$

This theorem is applicable, since

$$\text{Re}\ \lambda_i \neq \text{Re}\ \lambda_j + \text{Re}\ \lambda_k$$

for all eigenvalues of the saddle-focus at and near the 3DL homoclinic transition. This would allow one to easily obtain the Poincaré return map (20), but only permits to employ its first-order partial derivatives due to lack of smoothness. This would be sufficient to derive asymptotics for the fold and PD bifurcations of the primary limit cycles, as well as those for the secondary homoclinic orbits. However, to verify nondegeneracy conditions for LP and PD bifurcations and to detect codim 2 points, one needs higher-order partial derivatives of the return map Π. Their existence can be granted by using the C^k-linearization near the equilibrium with sufficiently big $k > 1$. This exists according to the C^k-linearization theorem by Sternberg [33], if one imposes a finite number of low-order non-resonance conditions on the eigenvalues, i.e.

$$\lambda_i \neq \sum_{j=1}^{4} n_j \lambda_j,$$

where $n_j \geqslant 0$ and $2 \leqslant \sum_{j=1}^{4} n_j \leqslant N$ for some $N = N(k)$ (see also [4, 34]). However, our analysis shows that such extra conditions can be avoided, similar to other homoclinic bifurcation scenarios [3].

For n-dimensional systems, generically the analysis of homoclinic bifurcations can be restricted to the *homoclinic center manifold*, a k-dimensional invariant finitely smooth manifold that is tangent at the equilibrium to the eigenspace corresponding to the union of all leading eigenvalues [14, 35–37]. Thus, k is the number of all leading eigenvalues of the equilibrium, counting their multiplicities. For the considered 3DL saddle to saddle-focus homoclinic transition case, we have $k = 4$. Thus, our analysis of 4D ODEs is sufficient to predict

the main features of the bifurcation diagram near this transition in a generic n-dimensional situation. However, some 'gap' conditions should be imposed on the eigenvalues of the critical equilibrium to guarantee more than C^1 smoothness of the homoclinic center manifold that is needed for bifurcation analysis. Whether or not one can avoid using the homoclinic center manifold requires further analysis.

It will also be interesting to study n-homoclinic orbits with $n \geqslant 2$ near the considered bifurcation and, in particular, investigate whether they could be degenerate. Another challenge would be to prove analytically the existence of infinite sequences of GPD points and strong resonances (see figure 7), at least for the truncated 3D model map (22). An interesting research direction is also to study the homoclinic 3DL transition in volume-preserving 4D ODEs, where it is always wild and has codim 1.

Acknowledgments

The authors are thankful to Andrey Shilnikov (Georgia State University, Atlanta), Heinz Hanssmann and Ferdinand Verhulst (Utrecht University) for their useful comments and discussions. We are also thankful to the two anonymous reviewers for careful reading of the original paper and their suggestions.

References

[1] Arnold V I, Afrajmovich V S, Il'yashenko Y S and Shil'nikov L P 1999 *Dynamical Systems 5: Bifurcation Theory and Catastrophe Theory* (Berlin: Springer) (https://doi.org/10.1007/978-3-642-57884-7)
[2] Ilyashenko Y and Li W 1999 *Nonlocal Bifurcations* (*Mathematical Surveys and Monographs* vol 66) (Providence, RI: American Mathematical Society) (https://doi.org/10.1090/surv/066)
[3] Shilnikov L P, Shilnikov A L, Turaev D and Chua L O 2001 *Methods of Qualitative Theory in Nonlinear Dynamics. Part* II (*World Scientific Series on Nonlinear Science. Series A: Monographs and Treatises* vol 5) (Singapore: World Scientific) (https://doi.org/10.1142/4221)
[4] Homburg A and Sandstede B 2010 Homoclinic and heteroclinic bifurcations in vector fields *Handbook of Dynamical Systems* vol 3, ed H W Broer *et al* (Amsterdam: Elsevier) pp 379–524
[5] Shil'nikov L P 1965 A case of the existence of a denumerable set of periodic motions *Dokl. Akad. Nauk SSSR* **160** 558–61
[6] Afraimovich V S, Gonchenko S V, Lerman L M, Shil'nikov A L and Turaev D V 2014 Scientific heritage of L P Shilnikov *Regul. Chaotic Dyn.* **19** 435–60
[7] Gonchenko S V, Turaev D V, Gaspard P and Nicolis G 1997 Complexity in the bifurcation structure of homoclinic loops to a saddle-focus *Nonlinearity* **10** 409–23
[8] Champneys A R and Kuznetsov Y A 1994 Numerical detection and continuation of codimension-two homoclinic bifurcations *Int. J. Bifurcation Chaos Appl. Sci. Eng.* **4** 785–822
[9] Kuznetsov Y A 1994 Impulses of a complicated form in models of nerve conduction *Sel. Math.* **13** 127–42
[10] Kuznetsov Y A, De Feo O and Rinaldi S 2001 Belyakov homoclinic bifurcations in a tritrophic food chain model *SIAM J. Appl. Math.* **62** 462–87
[11] Belyakov L A 1981 The bifurcation set in a system with a homoclinic saddle *Math. Notes* **28** 910–6
[12] Meijer H G E and Coombes S 2014 Travelling waves in models of neural tissue: from localised structures to periodic waves *EPJ Nonlinear Biomedical Physics* **2**
[13] Mira C and Carcassès J-P 1991 On the 'crossroad area–saddle area' and 'crossroad area–spring area' transitions *Int. J. Bifurcation Chaos Appl. Sci. Eng.* **1** 641–55
[14] Shilnikov L P, Shilnikov A L, Turaev D V and Chua L O 1998 *Methods of Qualitative Theory in Nonlinear Dynamics. Part* I (*World Scientific Series on Nonlinear Science. Series A: Monographs and Treatises* vol 4) (Singapore: World Scientific) (https://doi.org/10.1142/3707)
[15] Deng B 1989 The Šil'nikov problem, exponential expansion, strong λ-lemma, C^1-linearization, and homoclinic bifurcation *J. Differ. Equ.* **79** 189–231
[16] Deng B 1989 Exponential expansion with Šil'nikov's saddle-focus *J. Differ. Equ.* **82** 156–73

[17] Deng B 1996 Exponential expansion with principal eigenvalues: nonlinear dynamics, bifurcations and chaotic behavior *Int. J. Bifurcation Chaos Appl. Sci. Eng.* **6** 1161–7
[18] Govaerts W, Ghaziani R K, Kuznetsov Y A and Meijer H G E 2007 Numerical methods for two-parameter local bifurcation analysis of maps *SIAM J. Sci. Comput.* **29** 2644–67
[19] Neirynck N, Al-Hdaibat B, Govaerts W, Kuznetsov Y A and Meijer H G E 2016 Using MatContM in the study of a nonlinear map in economics *J. Phys.: Conf. Ser.* **692** 012013
[20] Kuznetsov Y A 2004 *Elements of Applied Bifurcation Theory* (*Applied Mathematical Sciences* vol 112) 3rd edn (New York: Springer)
[21] Dhooge A, Govaerts W and Kuznetsov Y A 2003 Matcont: a MATLAB package for numerical bifurcation analysis of ODEs *ACM Trans. Math. Softw.* **29** 141–64
[22] De Witte V, Govaerts W, Kuznetsov Y A and Friedman M 2012 Interactive initialization and continuation of homoclinic and heteroclinic orbits in MATLAB *ACM Trans. Math. Softw.* **38** 18
[23] Lorenz E N 1963 Deterministic nonperiodic flow *J. Atmos. Sci.* **20** 130–41
[24] Stenflo L 1996 Generalized Lorenz equations for acoustic-gravity waves in the atmosphere *Phys. Scr.* **53** 83
[25] Xavier J C and Rech P C 2010 Regular and chaotic dynamics of the Lorenz–Stenflo system *Int. J. Bifurcation Chaos Appl. Sci. Eng.* **20** 145–52
[26] Van Gorder R A 2013 Shil'nikov chaos in the 4D Lorenz–Stenflo system modeling the time evolution of nonlinear acoustic-gravity waves in a rotating atmosphere *Nonlinear Dyn.* **72** 837–51
[27] Rech P C 2016 Spiral organization of periodic structures in the Lorenz–Stenflo system *Phys. Scr.* **91** 075201
[28] Champneys A R, Kuznetsov Y A and Sandstede B 1996 A numerical toolbox for homoclinic bifurcation analysis *Int. J. Bifurcation Chaos Appl. Sci. Eng.* **6** 867–87
[29] Barrio R, Shilnikov A and Shilnikov L 2012 Kneadings, symbolic dynamics and painting Lorenz chaos *Int. J. Bifurcation Chaos Appl. Sci. Eng.* **22** 1230016
[30] Xing T, Barrio R and Shilnikov A 2014 Symbolic quest into homoclinic chaos *Int. J. Bifurcation Chaos Appl. Sci. Eng.* **24** 1440004
[31] Belyakov L A 1985 Bifurcations of systems with a homoclinic curve of the saddle-focus with a zero saddle value *Math. Notes* **36** 838–43
[32] Belitskii G R 1979 *Normal Forms, Invariants, and Local Mappings* (Kiev: Naukova Dumka) (in Russian)
[33] Sternberg S 1958 On the structure of local homeomorphisms of Euclidean *n*-space. II *Am. J. Math.* **80** 623–31
[34] Bronstein I U and Kopanskiĭ A Y 1994 *Smooth Invariant Manifolds and Normal Forms* (*World Scientific Series on Nonlinear Science. Series A: Monographs and Treatises* vol 7) (Singapore: World Scientific)
[35] Homburg A J 1996 Global aspects of homoclinic bifurcations of vector fields *Mem. Am. Math. Soc.* **121** 578
[36] Shashkov M V and Turaev D V 1999 An existence theorem of smooth nonlocal center manifolds for systems close to a system with a homoclinic loop *J. Nonlinear Sci.* **9** 525–73
[37] Sandstede B 2000 Center manifolds for homoclinic solutions *J. Dyn. Differ. Equ.* **12** 449–510